12-1995

Electrical Characterization of 4H-Silicon Carbide P-N Junction Diodes

Michael E. Dunn

ELECTRICAL CHARACTERIZATION OF 4H-SILICON CARBIDE P-N JUNCTION DIODES

THESIS

Michael E. Dunn, B.S.
2nd Lieutenant, USAF
AFIT/GAP/ENP/95D-04

DEPARTMENT OF THE AIR FORCE
AIR UNIVERSITY
AIR FORCE INSTITUTE OF TECHNOLOGY

Wright-Patterson Air Force Base, Ohio

DISCLAIMER NOTICE

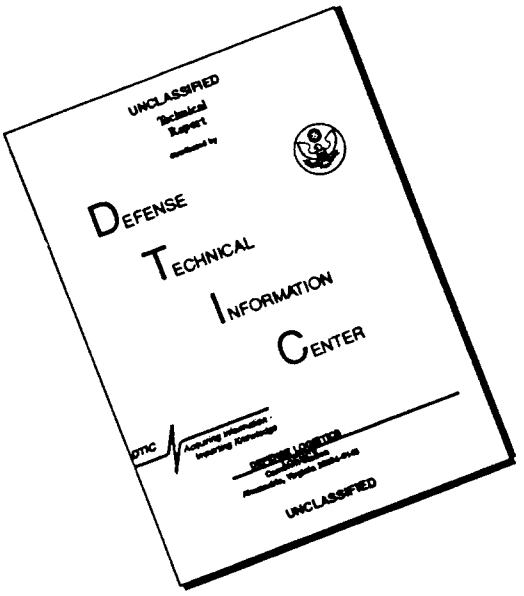

THIS DOCUMENT IS BEST QUALITY AVAILABLE. THE COPY FURNISHED TO DTIC CONTAINED A SIGNIFICANT NUMBER OF PAGES WHICH DO NOT REPRODUCE LEGIBLY.

AFIT/GAP/ENP/95D-04

ELECTRICAL CHARACTERIZATION OF

4H-SILICON CARBIDE P-N JUNCTION DIODES

THESIS

Michael E. Dunn, B.S.
2nd Lieutenant, USAF
AFIT/GAP/ENP/95D-04

Approved for public release; distribution unlimited

AFIT/GAP/ENP/95D-04

ELECTRICAL CHARACTERIZATION OF 4H-SILICON CARBIDE P-N JUNCTION DIODES

THESIS

Presented to the Faculty of the Graduate School of Engineering

of the Air Force Institute of Technology

Air University

in Partial Fulfillment of the Requirements for the Degree of

Master of Science in Engineering Physics

Michael E. Dunn, B.S.

2nd Lieutenant, USAF

December 1995

AFIT/GAP/ENP/95D-04

ELECTRICAL CHARACTERIZATION OF 4H-SILICON CARBIDE P-N JUNCTION DIODES

Michael E. Dunn, B.S.
2nd Lieutenant, USAF

Approved:

Yung Kee Yeo — 29 Nov '95
Dr. Yung K. Yeo, Chairman

Robert L Hengehold — 4 Dec '95
Dr. Robert L. Hengehold

Kitt C. Reinhardt — 4 DEC '95
Dr. Kitt C. Reinhardt

Acknowledgments

I would like to take this section to thank the people that have guided and supported me through the thesis process. First, I would like to thank my thesis advisors Dr. Yeo and Dr. Hengehold for the guidance they have given me on this project. Their insight and enjoyment of solid state physics, which was apparent in their classes, peaked my interests and persuaded me to choose a thesis in the solid state arena.

Without the help of Dr. Kitt Reinhardt at the Wright Laboratory my thesis would not have been possible. As my contact at Wright Labs and a committee member he not only provided the equipment and funding necessary for this research, but was also a mentor guiding me through the day to day research and writing process. I would also like to thank Mr. Chris Tunstall, the laboratory technician who helped me set-up the test equipment, kept me from breaking too many things, and worked to fix things that did go wrong. I would like to thank Mr. Jim Scofield who took the DLTS data that I used, and was always available to answer questions and explain results. Above all I would like to thank my parents and grandparents for their love and unwavering support.

Michael E. Dunn

Table of Contents

List of Tables

Table of Figures

Abstract

The current conduction mechanisms of 4H-SiC p^+n mesa diodes were studied using current-voltage-temperature (I-V-T), capacitance-voltage-temperature (C-V-T), deep level transient spectroscopy (DLTS), optical observations, and reverse breakdown measurements. Temperature and voltage dependencies of diffusion, recombination, and tunneling current processes are shown to be consistent with Sah-Noyce-Shockley theory. Recombination currents having an ideality factor of A=1.85-2.1 yielded an activation energy of E_A=1.56 eV, whereas for ideal recombination, A=2 and E_A=1.6 eV. Forward I-V curves of poor diodes dominated by tunneling and recombination processes, showing low reverse breakdown voltages of ~100 V, can be correlated to DLTS results which show large defect concentrations, and spectral observations indicating radiative recombination via defect sites. On the other hand, well-behaved diodes exhibited a breakdown voltage at ~450 V, a spectral output centered at ~385 nm, and recombination-to-diffusion current ratios of 10^{12}-10^{29} that agree with theory. C-V-T, DLTS, and reverse I-V-T data revealed several defect centers. C-V-T and reverse I-V-T measurements yielded an energy level at ~70 and ~62 meV, respectively, which is possibly attributable to nitrogen donor levels. Reverse I-V-T and DLTS results, in approximately half of the diodes tested, yielded a second trap level at 173 ± 19 and 150 ± 34 meV, respectively. Approximately 20% of the well-behaved diodes tested were found to breakdown unexpectedly at reverse biases as low as 95 V. It is believed that this unexpected breakdown is due to nanopipe defects in the diodes.

ELECTRICAL CHARACTERIZATION OF 4H-SILICON CARBIDE P-N JUNCTION DIODES

I. Introduction

Modern day electronics are the result of over 50 years of research and development. The advent of the first semiconductor devices can be traced back to the late 1890's, when selenium was used to form point-contact rectifying diodes. These devices were very leaky and produced excess heat that generally led to device failure. In the mid 1940's, point-contact silicon and germanium diodes were developed and used for radio and microwave detection. In 1947, the point-contact transistor was invented by researchers at Bell Laboratories, and the electronics era had begun (Mckelvey, 1993:443). The early transistors of 1947 had the same leaky current characteristics as the early point-contact rectifiers, and the need for a better transistor led to the development of the p-n junction in 1951.

The fundamental theory underlying p-n junction current voltage characteristics was first established by Shockley and developed in more depth by Sah, Noyce, and Shockley, and by Moll (Sze, 1981:63). Today, the p-n junction provides a building block for more complex solid-state devices, and a basic knowledge of p-n junction theory is vital to understanding the behavior of these devices.

Silicon has become the dominant semiconductor material used in commercial applications. As innovations in electronics continue, the development of better silicon

based electronic devices will be increasingly limited by material properties. Silicon's limitations have motivated research efforts in new materials that offer promises of superior performance. Wide-bandgap (WBG) semiconductors offer the possibility of significant improvements over the performance available with silicon semiconductors. One of these materials is silicon-carbide (SiC). SiC's wide-bandgap and high saturation velocity give the capability for producing devices that can operate at higher temperatures, frequencies, currents, and voltages than can Si devices. Therefore, a logical progression in the development of advanced performance electronics is the study of WBG p-n diodes.

Air Force Needs of Wide-Bandgap Electronics

The Air Force has a vested interest in the advancement of solid-state technology. For over 40 years, improvements in electronics have given the United States Air Force the most sophisticated and functional avionics systems in the world (Reinhardt, 1995). Recently WBG semiconductors have gained attention as candidates for use in military electronic applications. The Propulsion and Power Directorate at the Wright Laboratory, WPAFB has identified SiC as a prime candidate for use in the Air Force and Navy More Electric Aircraft (MEA) initiative. The MEA initiative seeks to replace aircraft hydraulic systems with electronic systems, shown in Figure 1. MEA system level payoff studies for the F-18 and F-16 have shown that replacing hydraulic systems with electronic systems will provide advances in reliability, vulnerability, weight, maintenance, and fuel consumption (Eicke, 1992), (Shah, 1992). However, removal of hydraulics eliminates the active cooling system for the aircraft, resulting in operating temperatures as high as

350 °C (Reinhardt, 1995), which exceeds the Si device maximum operating temperature of approximately 125 °C, and thus, highlights the need for high temperature WBG semiconductor devices.

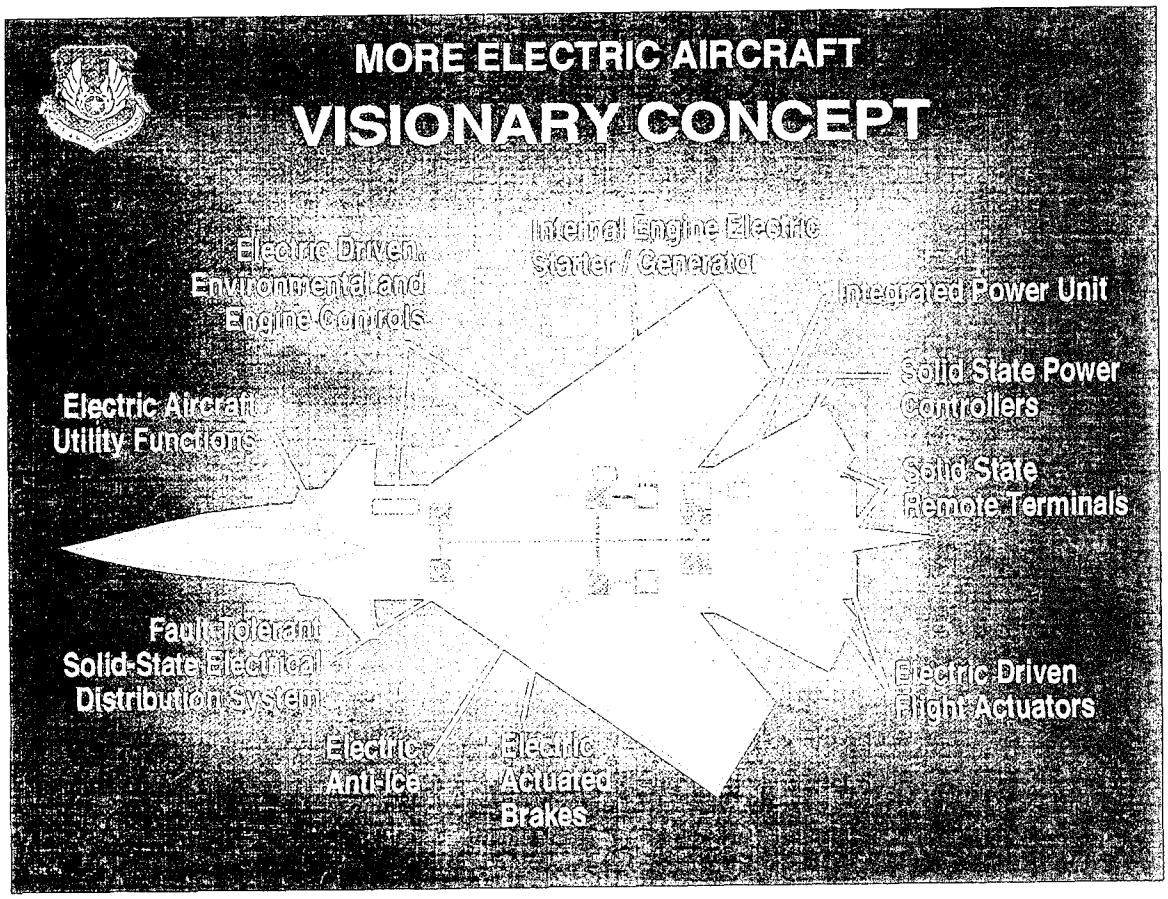

Figure 1. Depiction of aircraft hydraulic systems to be replaced with high temperature electronics using wide bandgap semiconductors.

Presently the military meets the thermal requirements for electronic systems operating at high temperatures by using large environmental control units (ECUs) (Scofield, 1993:3). ECUs are used in all modern aircraft and satellites in order to cool

the electronics. In the case of satellites, ECUs make up a substantial portion of satellite weight. They increase the in-space power requirements, and limit satellite lifetimes due to high failure rates. The cost associated with cooling electronic systems that are not designed to withstand higher temperatures is projected to increase dramatically as Air Force vehicles are built with more electronics and are operated in more extreme thermal conditions.

Heat on a spacecraft can only be eliminated by radiation. The rate of removal of radiation is proportional to the radiator area times the absolute temperature of the radiator to the fourth power as $R = AT^4$. Therefore, satellite electronics that can operate at 325 ^{o}C will radiate 5 times faster than one which operates at 125 ^{o}C, decreasing the ECU area required by a factor of 5. Currently, the weight of ECU systems are too great to build in redundancy. Thus, ECU failures limit satellite lifetimes. Replacing Si electronics with SiC devices would allow the reduction of ECU area, which in turn decreases in-flight power requirements, yields longer satellite lifetimes due to the ability to add in some redundant systems, and gives lower launch weights. An additional benefit is the ability of SiC to survive for longer periods in a radiation environment. Thus, replacing Si electronics with radiation resistant SiC electronics and subsequently down-sizing ECU systems would have cost benefits in nearly all Air Force vehicle systems due to lower maintenance costs and longer lifetimes.

Silicon-Carbide

The theoretical advantages of SiC's electrical properties have been known for over twenty years. Until recently, wafers could not be grown "clean" enough to yield devices that could realize SiC's electrical advantages. Recent innovations in crystal growth methods have significantly improved the quality and availability of 4H- and 6H-SiC wafers. Cree Research has been using a vapor transport technique, that was developed at North Carolina State University. These advances in the quality of crystal growth, combined with the already established industry in silicon, make SiC the leading candidate for large-scale production of wide-bandgap devices.

One of the advantages of SiC over other wide-bandgap semiconductors such as GaN is that it can be thermally oxidized to form a SiO_2 insulating layer that is suitable for metal-oxide-semiconductor (MOS) devices. MOS devices form the basis for Metal-Oxide-Semiconductor Field-Effect-Transistors (MOSFETs), which are used in large-scale integrated circuits such as semiconductor memories and microprocessors (Sze 1985:186). MOS device performance is currently limited by defects at the interface. These defects must be characterized and identified to further improve device quality (Reinhardt et al., 1995:6). To this end, Wright Laboratories is conducting in-house research in order to characterize bulk and epitaxial material.

Problem Statement

In order to help work towards achieving the Air Force goals of the MEA initiative, 4H-SiC p^+n junction diodes were studied. This research consists of the characterization of current conduction mechanisms and identification of defect levels within the bandgap.

Data was obtained using current-voltage-temperature (I-V-T), capacitance-voltage-temperature (C-V-T), deep level transient spectroscopy (DLTS), and reverse breakdown measurement techniques. It is hoped that this research will help provide the information needed to make SiC operational.

Thesis Organization

This thesis is divided into six chapters. The first chapter outlines the motivation and scope of the research completed. The second chapter contains the theory of SiC growth, crystalline properties, electrical properties, and p-n diode current conduction. Chapter three describes the experimental equipment and test procedures used to take data. In chapter four, the techniques used to analyze the data are presented, accompanied by a discussion of the results. Lastly, chapter five contains a summary of the results and gives recommendations for future research.

II. Theory

Wide Bandgap Semiconductors

The performance of a device operating at high temperatures is limited by the material's energy bandgap, intrinsic carrier concentration, electron and hole effective masses, and carrier mobilities. It will be shown that it is impossible for silicon based devices to operate much above 525 K due to their narrow bandgap. Equation (2.1) shows that for an intrinsic (undoped) semiconductor, the reverse leakage current is proportional to the intrinsic carrier concentration, n_i, squared. In turn, the ideal intrinsic carrier concentration is dependent on the semiconductor bandgap, E_g, the operating temperature, T, the Boltzman constant, k, and the density of states in the conduction band and valence band denoted by N_c and N_v, respectively, as

$$I_o \propto n_i^2 = (N_c N_v)\exp\left(\frac{-E_g}{kT}\right). \tag{2.1}$$

The leakage current is due to minority carriers, electrons and holes on the p and n-side , respectively, being thermally excited to the conduction and valence bands, respectively. N_c and N_v can be calculated from

$$N_c = 2M_c\left[\frac{2\pi m_n kT}{h^2}\right]^{\frac{3}{2}} \tag{2.2}$$

and

$$N_v = 2\left[\frac{2\pi m_p kT}{h^2}\right]^{\frac{3}{2}}, \tag{2.3}$$

where m_n and m_p are the electron effective mass and the hole effective mass, respectively, M_c is the number of conduction band minima in the first Brillouin zone, and h is Planck's constant.

Using Eqs. (2.1)-(2.3), one can determine the maximum operating temperature for two different semiconductors for a given hypothetical maximum allowable leakage current. A comparison between silicon and silicon-carbide will illustrate the superiority of WBG semiconductors in high temperature operation. Silicon has an energy gap of 1.12 eV with established values for N_c and N_v of 2.8×10^{19} cm^{-3} and 1.04×10^{19} cm^{-3}, respectively. 4H-SiC has a bandgap of 3.2 eV and an electron effective mass of $0.191 m_o$, where m_o is the electron rest mass. Recent research has established that 4H-SiC most likely has 12 conduction band minima (Gotz, 1993:3336), leading to the value $N_c = 8.39 \times 10^{18}$ cm^{-3}. Published values of hole effective masses for 4H-SiC could not be found. For this example it was assumed that SiC has a N_v value that is approximately half N_c, like Si and Ge, yielding $N_c = 4.2 \times 10^{18}$ cm^{-3}. Given these numbers, the intrinsic carrier concentrations of Si and 4H-SiC are plotted as a function of temperature in Figure 2. The Si and 4H-SiC lines intersect the arbitrarily chosen maximum carrier concentration of 3.4×10^{26} cm^{-3} at 435 K and 1337 K, respectively. Therefore, all else being equal, SiC offers a dramatic improvement in performance over Si. This superior performance at high temperature is due chiefly to the large bandgap of SiC. Examining Eq. (2.1), one can qualitatively see that with bandgaps of 1.12 eV and 3.2 eV for Si and 4H-SiC, respectively, the SiC semiconductor can operate at approximately 3 times

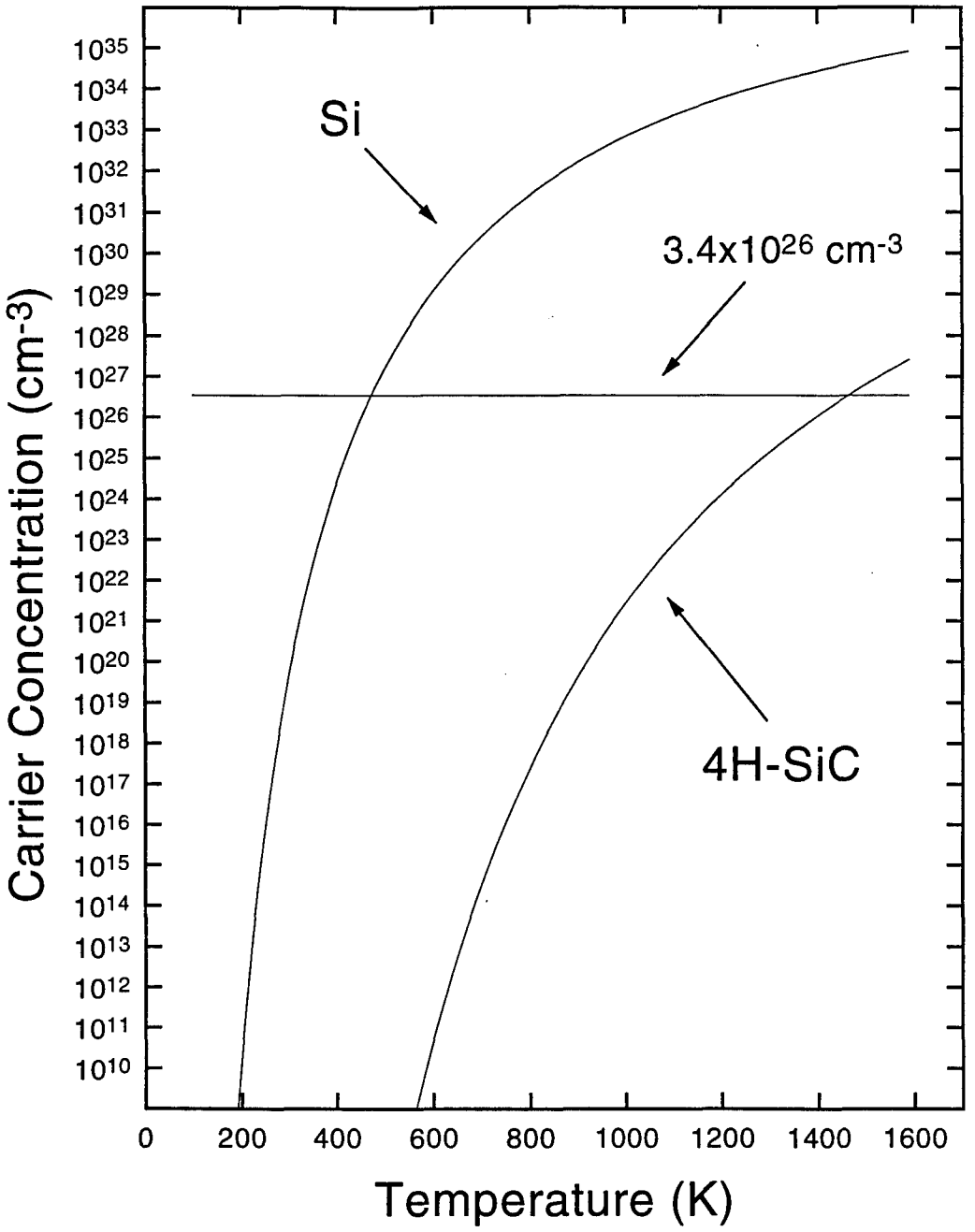

Figure 2. A comparison of the free carrier concentrations of Si and 4H-SiC versus the operating temperature (K). The Si and 4H-SiC lines are solid and dashed, respectively.

the temperature of the Si semiconductor for a given maximum allowable leakage current.

In the case of extrinsic, or doped, semiconductors, Eq. (2.1) is not accurate at low temperatures. However, at higher temperatures a semiconductor's total carrier concentration approaches the intrinsic carrier concentration. Eq. (2.4) determines the carrier concentration for a semiconductor doped with donors,

$$n = \frac{N_D}{2} + \left[\frac{N_D^2}{4} + n_i^2\right]^{1/2}, \tag{2.4}$$

where n is the carrier concentration, and N_D is the doping density of donors. Eq. (2.4) and Figure 3 show that with increasing temperature, an extrinsic semiconductor becomes intrinsic as $n_i >> N_D$ and $n \rightarrow n_i$. Figure 3 can be explained by considering the two sources of carriers. Electrons located in shallow donor levels, and also electrons in the valence band, can be excited up to the conduction band. At very low temperatures n = 0, but as the temperature is increased weakly bound electrons from the donor atoms are easily excited up into the conduction band. As the temperature increases, more donor electrons are excited until $n = N_D$, and there are no more donor electrons to excite. The large excitation energy of valence band electrons produces a flat region in the curve, where all the donor electrons are in the conduction band but no valence electrons are excited. When the temperature gets high enough, valence electrons are excited and the carrier concentration increases again. At the high temperatures where we are interested, the carrier concentration asymptotically approaches the intrinsic carrier concentration curves as shown in Figure 3.

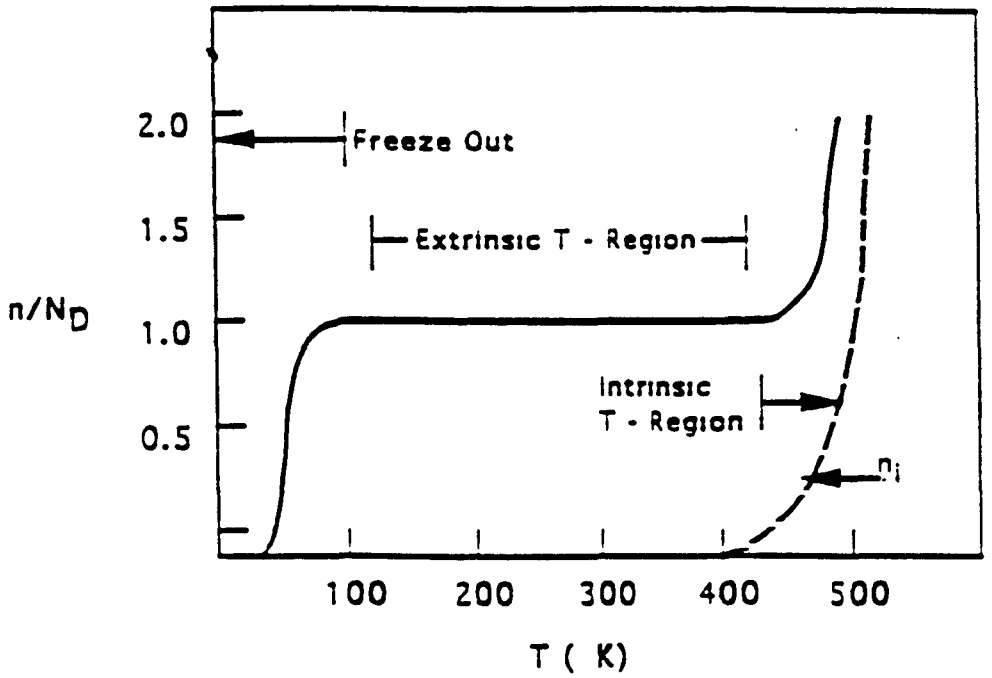

Figure 3. Comparison of the carrier concentrations of an intrinsic and an extrinsic semiconductor vs. temperature.

One can conclude from Eqs. (2.1)-(2.4) and Figures 2 and 3 that regardless of other electrical properties such as drift mobility, carrier lifetimes, effective masses, diffusion lengths, dielectric constant, and electron saturation drift velocity, there is no conceivable way to make a narrow bandgap semiconductor operate at higher temperatures. The only solution is developing WBG semiconductors while keeping the aforementioned electrical properties in mind when choosing the semiconductor material.

Electrical Properties of SiC

The electrical properties of SiC are outstanding. The advantages over Si are great enough to warrant studying and developing SiC for room temperature applications alone. This section will compare the properties of 4H-SiC to those of Si and GaAs, two common semiconductor materials. The energy bandgap of 4H-SiC is 3.2 eV, while Si

and GaAs have bandgaps of 1.12 and 1.43 eV, respectively. The larger bandgap, as discussed previously, allows an operating temperature that is approximately 3 times that of Si, and over 2 times that of GaAs.

The electric field at which SiC breaks down is over 7 times greater than that of both Si and GaAs. Material failure occurs when high reverse-biases cause avalanche breakdown. A greater electric field breakdown allows the production of thyristors, power diodes, and power transistors that can operate at higher voltages and higher powers.

SiC has a high saturated electron drift velocity. The electron drift velocity of SiC is over 2 times that of Si and GaAs. The electron drift velocity is the speed at which electrons travel at a given applied potential. Associated with this high saturated electron drift velocity are the following properties: greater mobilities, better conductivity, more efficient operation under constant bias, faster frequency switching, and less power loss when switching. The more efficient operation and less power loss in switching reduce the power requirements for running these devices and decrease the amount of waste heat created during operation.

The thermal conductivity of SiC exceeds that of Si and GaAs by over 3 and 9 times, respectively. So, in addition to producing less heat, SiC will dissipate the produced heat faster. (Scofield, 1993:13)

Crystalline Structure

SiC has been shown to be stable in over a hundred different crystal configurations, known as polytypes. A given polytype can be differentiated from other polytypes by the

stacking pattern of the tetrahedrally bonded Si-C bi-layers along the c-axis. Each stacking sequence has slightly different physical and electrical characteristics, even though given one single atom, every polytype is nearly indistinguishable out to the nearest neighbors. Going out to the second and third nearest neighbor shells, however, results in inequivalent lattice sites for different polytypes. Given two bi-layers, they can be stacked in a wurtzite (hexagonal) or a zinc-blende (cubic) arrangement. Different combinations of wurzite and zinc-blende bi-layers yield different polytypes.

The three SiC polytypes showing the most promise are 3C, 4H, and 6H, where the number refers to the number of bi-layers until the stacking pattern is repeated, and C or H refers to cubic or hexagonal. 6H-SiC is the easiest of the three to make, but 3C and 4H have shown superior electrical properties. These different stacking patterns are shown in Figure 4 (Morkoc et al., 1994:1336), where Morkoc et al. has arbitrarily assigned the letters A, B, and C to each layer that has a unique arrangement with respect to the others. Subsequent layers are assigned letters depending on their symmetry with the original three layers. 3C-SiC is purely cubic, where (k) denotes cubic symmetry. 4H-SiC, the polytype researched, is half cubic (k) and half hexagonal (h). 6H-SiC, the most common polytype, is two-thirds cubic (k_1 and k_2), and one-third hexagonal (h_1). Both silicon and carbon are located in Column IV of the periodic table, dictating a tetravalent bonding structure and covalent electron-pair bonds between neighboring atoms (McKelvey, 1993:22). Quantum theory has shown that electron-pair covalent bonds form a strong

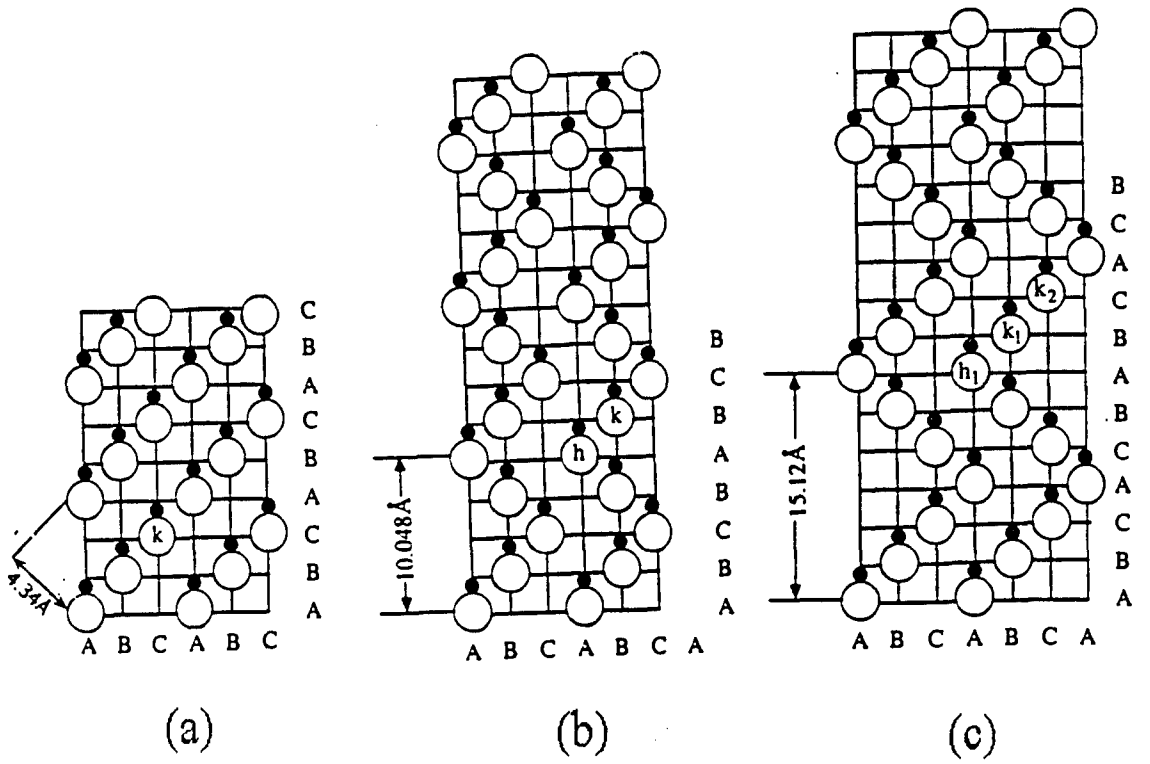

Figure 4. Crystal structures of silicon-carbide polytypes (a) 3C, (b) 4H, and (c) 6H.

link between neighboring atoms. As a result, SiC is very hard and strong. Elements in Column IV are semiconductors as a direct result of covalent bonding. For 4H-SiC, cell lengths are

c = 10.05 Angstroms and a = b = 3.076 Angstroms,

where c is the distance of one cell along the c-axis, and one cell contains 4 layers. The axial ratio of c/(4a) = 0.8168 is very close to the ideal value of 0.8165 (Scofield, 1993:11).

SiC Crystal Growth

The 4H-SiC samples used for this thesis were made by Cree Research Inc. They were grown using a sublimation, sometimes called vapor transport, technique. This growth technique was developed by North Carolina State University and Cree with Navy funding. In sublimation growth, a SiC seed crystal is hung over Si and C vapor. The seed crystal is kept at approximately 2050 K while bulk Si and C are vaporized with a 2250 K heat source. The Si and C vapor sublimes on the seed crystal, and the crystal grows downwards. In the past, the major defects in substrates grown by sublimation are so called micropipes that extend down the crystal boule. Two different mechanisms for micropipe formation have been suggested. The first is that the micropipes form due to contaminants introduced during the sublimation process. The second theory, reported by Wang and referenced by Neudeck, is that the micropipes are "open super screw dislocations" that extend down the c-axis of the crystal during growth (Wang et al., 1993:307). Research has shown that these micropipe defects cause pre-avalanche reverse-bias point failures in p-n junctions (Neudeck and Powell, 1994:63). Cree has been able to reduce the density of micropipes in 4H and 6H-SiC to 100/cm^2. This is an improvement, however, until the micropipe problem can be completely solved, SiC devices will be limited in size and quality.

P-N Junction Diode Theory and Current Conduction Mechanisms

The key to understanding a specific diode's shortcomings is to understand the current conduction mechanisms. In p-n diodes several current transport mechanisms may occur at the same time. The ideal diode's dark current conduction, described by

Shockley, is due only to diffusion (Shockley, 1949:435). This is generally not observed in experiment. No semiconductor is perfectly pure. As a result of impurities and lattice defects, energy levels will exist between the valence and conduction bands. These levels allow various other current conduction mechanisms to occur. It follows that fewer impurities and lattice defects give an I-V curve that more closely approximates Shockley's ideal case.

Current conduction in Si due to two exponential terms was first reported by Wolf, and later referenced by Reinhardt (Wolf et al., 1977:419). Wolf identified the two exponential terms as diffusion and junction space-charge recombination of the Shockley-Read-Hall type (Sah et al., 1957:1228). It was later found that the inclusion of shunt and series resistance terms, R_{sh} and R_s, respectively, produced a current-conduction model which more closely matched experimental results. The current-conduction model is given by

$$J_{total} = J_{dif}\left[\exp\left(\frac{qV_D}{A_1kT}\right)-1\right]+J_{rec}\left[\exp\left(\frac{qV_D}{A_2kT}\right)-1\right]+\frac{V_D}{R_{sh}}. \qquad (2.5)$$

Where J_{total} is the total current density, J_{dif} is the saturation current density for diffusion, and J_{rec} is the saturation current density for space-charge recombination. A_1 and A_2 are ideality factors. For the case of ideal diffusion, $A_1 = 1$. The value of A_2 is dependent on the location of recombination centers within the bandgap. If these recombination centers are located near the center of the bandgap, A_2 will have an approximate value of 2. The third term accounts for current due to shunting. When shunting is due to carrier tunneling

and capture-emission, then the shunting resistance term can be better modeled by

$$J_{sh} = J_o \exp (B\ V), \tag{2.6}$$

where J_o is the reverse-saturation current density due to tunneling (Banerjee and Anderson, 1986:38). Current mechanisms due to diffusion, recombination, and tunneling are shown in Figure 5 (Reinhardt, 1993:33).

The diode junction voltage, V_D, is related to the applied voltage, V, the total current, and the series resistance by

$$V_D = V - I_{total}R_s\,. \tag{2.7}$$

Multiplying Eq. (2.5) by the diode area and substituting in Eq. (2.7) yield a

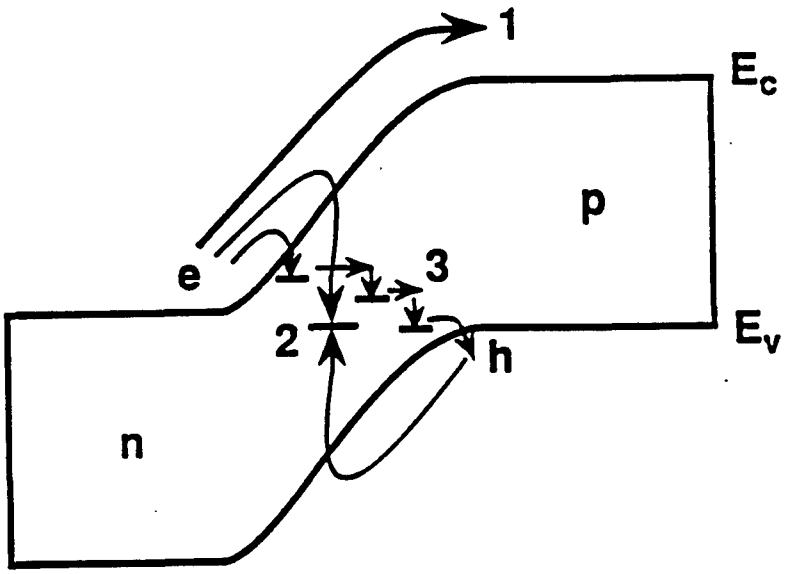

Figure 5. Diagram of a p-n junction current showing, (1) diffusion current, (2) recombination current through defect sites, and (3) tunneling current via multiple defect sites.

comprehensive current conduction model. However, this transcendental model is difficult to work with. The relative strength of the different current mechanisms is a function of the semiconductor's bandgap, minority carrier lifetimes on each side of the device, operating temperature, and the doping density. The theory of diffusion, recombination, and tunneling currents will be discussed in the three sections that follow.

Diffusion Current

Four assumptions were made in Shockley's development of a diffusion current model (Sze, 1981:84); (1) the p-n junction is abrupt, (2) the Boltzman approximation holds in the depletion region, (3) the injected minority carrier densities are negligible with respect to the majority carrier densities, and (4) the electron and hole currents are constant in the depletion layer, and the currents are not due to generation processes. The Boltzman approximation results in

$$n_n = n_i \exp\left[\frac{E_f - E_i}{kT}\right] \tag{2.8}$$

and

$$p_p = n_i \exp\left[\frac{E_i - E_f}{kT}\right], \tag{2.9}$$

where E_i is the intrinsic energy level, and p_p and n_n are the equilibrium majority hole and electron carrier densities, respectively. Considering these assumptions, the diffusion current can be expressed as

$$J_D = J_n + J_p = J_{dif}\left[\exp\left(\frac{qV}{kT}\right) - 1\right], \tag{2.10}$$

where $$J_D \approx J_{dif}\left[\exp\left(\frac{qV}{A_i kT}\right)\right] \qquad \text{for } qV >> kT, \tag{2.11}$$

and $$J_{dif} = q\left[\frac{n_p D_n}{L_n} + \frac{p_n D_p}{L_p}\right]. \tag{2.12}$$

J_{dif} is the reverse saturation diffusion current density. D_n, D_p, L_n, and L_p are the diffusion rates and diffusion lengths for electrons and holes, respectively, while n_p and p_n are the minority carrier densities on the p and n-side, respectively. Figure 6 illustrates a forward biased p-n diode for which this model is applicable (McKelvey, 1993:458). The diffusion current is labeled (1) in Figure 5 and J in Figure 6, and is due to majority carrier (electrons on the n-side and holes on the p-side) injection across the depletion region to the other side of the junction. After injection, the majority carriers become minority carriers and are able to recombine with majority carriers supplied by the external circuit.

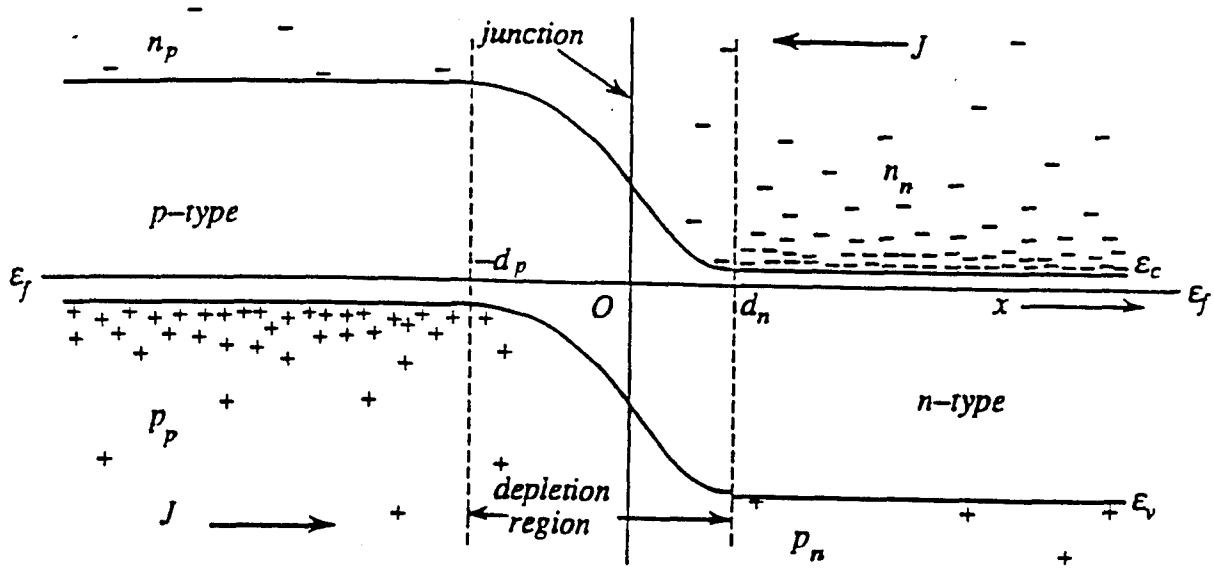

Figure 6. Typical p-n junction diode, showing electron and hole diffusion currents *J*.

Eq (2.11) assumes that qV >> kT, and includes the ideality factor, A_1, where A_1 will equal 1 in the case of ideal diffusion. The dependencies of Eqs. (2.11) and (2.12) can be seen more clearly by substituting in Eqs. (2.1)-(2.3), and using the relations for a p^+n diode, $n_p = n_i^2/N_A$, and $p_n=n_i^2/N_A$, yielding,

$$J_{dif} \propto T^3 \exp\left(\frac{-E_g}{kT}\right) \tag{2.13}$$

and

$$J_D \propto J_{dif} \exp\left(\frac{qV}{kT}\right). \tag{2.14}$$

The equations show that J_{dif} has an exponential dependence on temperature and the bandgap, and J_D should increase exponentially with increasing voltage. These relationships will be used to fit lines to I-V plots in order to identify which portion of the I-V curves is due to diffusion currents.

For the diode depicted in Figure 6, it is noted that the depletion region extends farther into the p-side of the diode than into the n-side. This is due to the fact that the n-side of the diode has a higher doping density. There is a steep gradient of both electron and hole concentrations at the junction due to the different doping densities. The concentration gradients generate a diffusion flux of holes to the right and electrons to the left, leaving immobile acceptor and donor ions uncompensated (McKelvey, 1993:448). When one applies Poisson's equation to the potential field between the two sides of the junction, and considers the appropriate boundary conditions, it is found that

$$N_a d_p = N_d d_n, \tag{2.15}$$

where d_p and d_n are depicted in Figure 6. Thus, a p^+n diode, where p^+ indicates that $N_a>>N_d$, will have a depletion region that extends almost exclusively into the n-side of

the diode. This will be relevant when analyzing data taken using C-V-T and DLTS techniques.

In the ideal diode, only diffusion current will be seen. However, in general the ideal diffusion equation only gives qualitative agreement with the current-voltage curves from a sample. Departure of current-voltage characteristics from Shockley's diffusion model are due to: (1) surface effects, (2) generation and recombination of carriers in the depletion region, (3) tunneling of carriers at the interface through states in the bandgap, (4) high-injection current, (5) series resistance, and (6) junction breakdown at high enough voltages (Sze, 1981:90). In normal operating conditions, the departure of I-V curves from Shockley's diffusion model will be primarily due to generation and recombination currents.

Generation and Recombination Processes

Bulk generation and recombination. Bulk generation and recombination processes refer to generation and recombination that occurs exclusively on the p or n-side of the device rather than across the junction. When the thermal-equilibrium condition is disturbed such that $n_n p_n \neq n_i^2$ or $n_p p_p \neq n_i^2$, then recombination processes occur to restore equilibrium. For example, when excess carriers are injected into the semiconductor, equilibrium is restored by the recombination of majority and minority carriers. When recombination occurs, energy is released as a photon or as heat that goes into the crystal lattice. The first case is radiative recombination, whereas the second case is nonradiative recombination.

The recombination process can be direct or indirect. Direct recombination dominates in direct bandgap semiconductors such as GaAs, where a conduction band minima corresponds to a valence band maxima in momentum space. In indirect semiconductors such as Si and SiC, the conduction band minima and valence band maxima do not have corresponding locations in momentum space. As a result, a direct transition will not conserve both energy and momentum, and is therefore forbidden. Indirect transitions can only occur by the exchange of phonons with the crystal lattice or by recombining through a center located in the energy gap. According to Sze, in the case of indirect transitions, the dominant recombination process occurs via localized energy states in the energy gap. These energy states, often called recombination centers, act as "stepping stones" between the conduction and valence band (Sze, 1985:48).

Figure 7 illustrates the different transitions that can occur through a recombination center. The first process is called electron capture. In electron capture an electron in the conduction band drops down to the defect center. Using Fermi-Dirac statistics one finds that the probability of a center being occupied is

$$F = \frac{1}{1+\exp\left(\frac{E_t - E_f}{kT}\right)}, \tag{2.16}$$

where E_f is the Fermi energy level and E_t is the trap's energy level. The probability of a trap level not being occupied is (1-F). The rate of electron capture, c_n, is proportional to

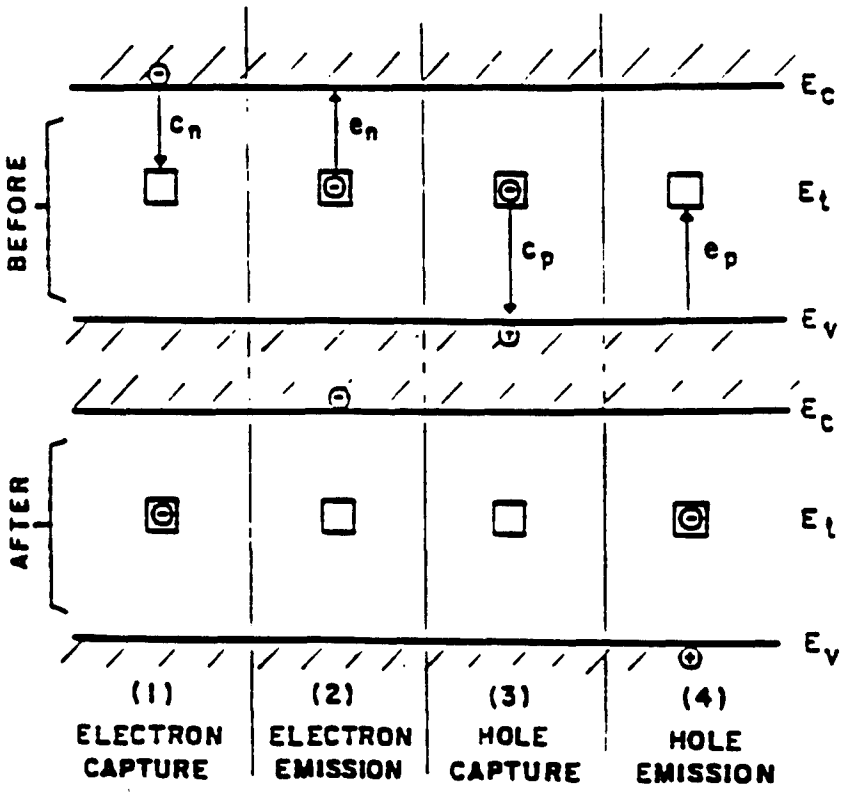

Figure 7. A diagram of generation and recombination processes occurring at thermal equilibrium.

the number of empty centers, since each center can hold one electron, and the number of electrons in the conduction band, n. The resulting equation is shown as

$$c_n = v_{th}\sigma_n n N_t (1-F), \tag{2.17}$$

where v_{th} is the thermal velocity of the carrier, N_t is the number of traps, and σ_n is the capture cross section. The capture cross section is an indicator of how probable it is that a carrier will be captured by a defect center. The second process in Figure 7 is electron emission, which is the opposite of electron capture. The electron emission rate, e_n, is proportional to the number of centers filled as shown by

$$e_n = \beta_n N_t F, \tag{2.18}$$

where β_n is the emission probability for the center. At equilibrium, the rate of capture and emission are equal allowing β_n to be solved for. Setting Eqs. (2.17) and (2.18) equal, and substituting Eq. (2.16) into the results, gives

$$\beta_n = v_{th}\ \sigma_n n_i e^{(E_t - E_i)/kT}. \tag{2.19}$$

It is interesting to note that the closer E_t is to the conduction band, the larger the emission probability becomes. The same concepts and general equations apply to exchanges between the valence band and a defect center, denoted as transitions (3) and (4) in Figure 7. The hole capture rate will be proportional to the number of centers which contain an electron as shown by

$$c_p = v_{th}\sigma_p p N_t F, \tag{2.20}$$

while the hole emission rate will be proportional to the number of centers empty as

shown by

$$e_p = \beta_p N_t (1-F). \tag{2.21}$$

The emission probability, β_p, for a hole is solved for in a manner identical to that which is described above for β_n and it is given by

$$\beta_p = v_{th}\sigma_p n_i e^{(E_i-E_t)/kT}. \tag{2.22}$$

In Eq. (2.22), we see that the hole emission probability will be larger the closer E_t is to the valence band edge. From Eqs. (2.19) and (2.22), it follows that efficient generation and recombination centers will be located in the middle of the bandgap, where $e_p \approx e_n$ and $c_p \approx c_n$, respectively.

For a given energy level within the bandgap, if $c_n >> c_p$, then the level is referred to as an "electron trap". Conversely, if $c_p >> c_n$, it is referred to as a "hole trap", and when $c_n \approx c_p$, the level is a "recombination center". The rate of carrier recombination, U, can be written using the emission and capture rates in Eqs. (2.17), (2.18), (2.20), and (2.21), yielding

$$U = -\frac{dn}{dt} = -\frac{dp}{dt} = c_n - e_n = c_p - e_p. \tag{2.23}$$

Substituting variables into these equations gives

$$U = \frac{\left(pn - n_i^2\right)N_t v_{th}\sigma_n\sigma_p}{\sigma_p\left[p + n_i \exp\left(\frac{E_i - E_t}{kT}\right)\right] + \sigma_n\left[n + n_i \exp\left(\frac{E_t - E_i}{kT}\right)\right]}, \tag{2.24}$$

or
$$U = \frac{\left(pn - n_i^2\right)}{\left[p + n_i \exp\left(\frac{E_i - E_t}{kT}\right)\right]\tau_p + \left[n + n_i \exp\left(\frac{E_t - E_i}{kT}\right)\right]\tau_n} . \quad (2.25)$$

Here τ_n and τ_p are the electron and hole recombination lifetimes, respectively, given by

$$\tau_n = \left(N_t v_{th} \sigma_n\right)^{-1} \quad (2.26)$$

and
$$\tau_p = \left(N_t v_{th} \sigma_p\right)^{-1} . \quad (2.27)$$

When examining Eqs. (2.24) and (2.25), it can be seen that the maximum rate of recombination occurs when $E_t \approx E_i$. To calculate the total current due to recombination, one integrates U(x,V) across the junction. After a lengthy derivation, one can obtain an open form of the recombination current which is valid for moderate forward-biases as

$$J_R \propto T^{\frac{5}{2}} \exp\left(-\frac{E_g}{2kT}\right) \exp\left(\frac{qv}{A_2 kT}\right). \quad (2.28)$$

Space-Charge-Layer Recombination and Generation. The general theory of bulk recombination can be applied to generation and recombination theory within the depletion region. Recombination of holes and electrons via defect centers within the depletion region causes a flow of current from the p to n-side of the junction. Junction recombination is labeled (2) in Figure 5. The bulk recombination equations are found to be applicable in the space charge layer if the Boltzmann approximation can be made. The Boltzmann approximation in Eqs. (2.4) and (2.5) was also used by Shockley to describe diffusion across the junction. Under reverse bias conditions, only junction generation currents exist due to the lack of free carriers in the depletion region, making the capture rates negligible.

Perimeter Recombination and Generation. A third recombination phenomena is surface recombination. The ending of the lattice structure at the surface of the semiconductor creates many localized energy states which act as generation-recombination centers. Surface recombination has a dramatic effect on some devices. The surface recombination rate per unit area is similar to Eq. (2.25), and is given by

$$U_s = \frac{\left(p_s n_s - n_i^2\right) N_{st} v_{th} \sigma_n \sigma_p}{\sigma_p \left[p_s + n_i \exp\left(\frac{E_i - E_t}{kT}\right)\right] + \sigma_n \left[n_s + n_i \exp\left(\frac{E_t - E_i}{kT}\right)\right]}, \tag{2.29}$$

where n_s and p_s are the electron and hole concentrations at the surface, and N_{st} is the surface recombination center density per unit area. For diodes having a relatively large number of centers along the perimeter, the perimeter recombination will dominate over bulk recombination effects. When this is the case, one should observe a greater portion of the I-V curve being due to recombination for smaller devices which have larger perimeter-to-area ratios.

Tunneling Current

Tunneling current is due to carriers tunneling through the junction to the other side, as shown for the process (3) in Figure 5. The different possible tunneling paths are shown in Figure 8. Horizontal transitions are due to tunneling, while vertical transitions are due to capture and emission processes. A majority carrier can tunnel all the way through the junction. It can tunnel via states within the forbidden gap, or some

combination of capture, emission, and tunneling can occur (Sze, 1981:528). The tunneling current density, as reported by Sze, is given by (Moll J.L., 1964:252)

$$J_t = \sqrt{\frac{2m^*}{E_g}}\frac{q^3\varepsilon_s V}{h^2}\exp\left(\frac{-8\pi\sqrt{2\,m^* E_g^{\,3/2}}}{3q\varepsilon_s h}\right), \tag{2.30}$$

where m^* is the effective mass, and ε_s is the permitivity of SiC.

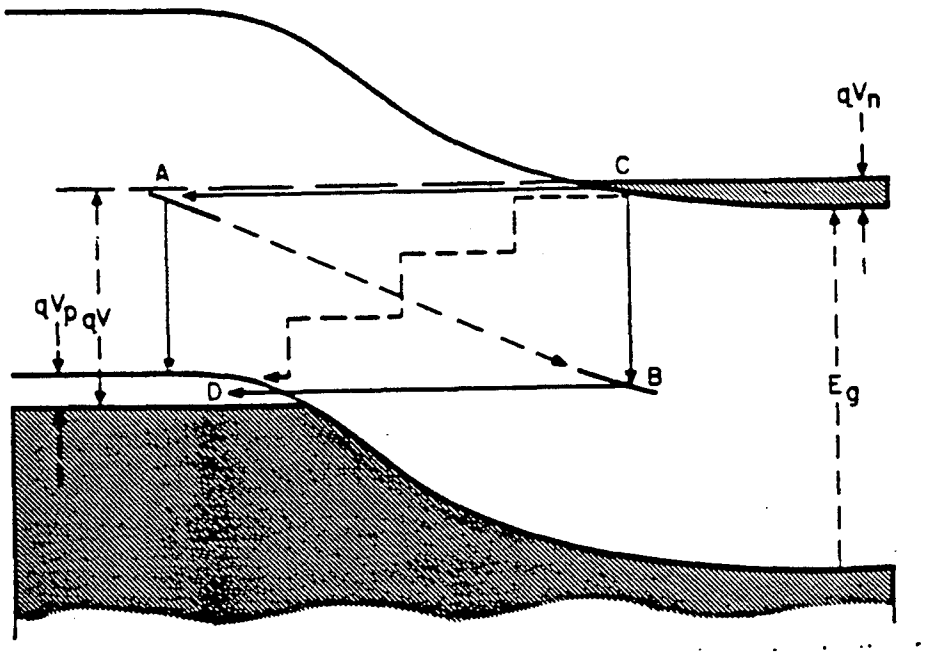

Figure 8. Energy band diagram showing tunneling mechanisms through defect states in the bandgap.

Tunneling and avalanche breakdown are the two reverse breakdown mechanisms of a diode. The energy bandgap of SiC is inversely proportional to temperature, while J_t has an inverse proportionality to energy bandgap. The result is that one can identify

breakdown due to tunneling when the breakdown voltage decreases with increasing temperature. Breakdown due to avalanche multiplication can be identified by its positive temperature coefficient (Sze, 1981:98).

Space-Charge-Layer (SCL) Capacitance

A capacitance exists across a p-n diode due to the ionization produced charge layers on either side of the junction. The size of the depletion region, $d_n + d_p$, in Figure 6 can be derived using Eq. (2.15). The derivation consists of integrating over the charge layers to determine the electric fields, and using Poisson's equations with the applicable boundary conditions, resulting in

$$W = d_n + d_p = \sqrt{\frac{2\varepsilon_s(N_A + N_D)V_{bi}}{qN_AN_D}}. \tag{2.31}$$

A more accurate form of Eq. (2.31) is obtained by including the correction factor of 2kT/q in order to account for the majority-carrier contribution to the SCL. Eq. (2.31) can be generalized by including an applied voltage term that varies the diode potential. In the case of a p^+n diode, $N_A >> N_D$, the N_D term in the numerator is negligible. These three changes produce a more workable form of Eq. (2.31) as given by

$$W = \sqrt{\frac{2\varepsilon_s}{qN_D}\left(V_{bi} - V - \frac{2kT}{q}\right)}. \tag{2.32}$$

Eq. (2.32) assumes a p^+n diode having an abrupt junction, and V is the voltage applied to the p-side of the diode (Sze, 1981:77). The diffusion potential or "built in potential," V_{bi}, can be calculated for given doping densities and Eq. (2.1) using

$$V_{bi} = \frac{kT}{q} \ln\left(\frac{N_A N_D}{n_i^2}\right). \tag{2.33}$$

Given an ideal one-sided abrupt junction with no defect levels, the capacitance is described by

$$C = \frac{\varepsilon_s S}{W} = S\sqrt{\frac{q\varepsilon_s N_D}{2}\left(V_{bi} - V - \frac{2kT}{q}\right)^{-1/2}}, \tag{2.34}$$

where S is the area of the junction. The more general form of the equation is

$$C \equiv \frac{dQ}{dV} \approx \frac{\Delta Q}{\Delta V}, \tag{2.35}$$

where dQ is a small change in charge per unit area due to an incremental change in applied voltage (Sze, 1981:79).

Eq. (2.34) will not adequately describe the capacitance characteristics of a diode if the diode is not abrupt, or if the diode has defect traps and recombination centers. In the case of defect traps,

$$C = S\sqrt{\frac{q\varepsilon_s\left[N_D - \sum_i N_i(t,T)\right]}{2}\left(V_{bi} - V - \frac{2kT}{q}\right)^{-1/2}}, \tag{2.36}$$

where N_i is the density of n-side defect level traps affecting the capacitance, and is dependent on the temperature, T, and the scan rate, t, at which the capacitance data is taken.

III. Equipment and Procedures

The devices tested are 4H-SiC p^+n diodes made by Cree Inc. The diodes were delivered as individual mesa diodes diced on a 1 1/2" wafer. The diodes are doped with nitrogen donors and aluminum acceptors. The nitrogen donors are located ~45 meV and ~105 meV below the conduction band for hexagonal and cubic sites, respectively. The aluminum acceptors are located at 240-250 meV, where the larger the doping density, the deeper the energy level. The p^+n diode structure and the diode package are shown in Figure 9. Forty-two diodes were selected from the diced wafer and packaged by Mr. Larry Callahan at the Electronics Directorate Wright Laboratory. The diodes were mounted and wire bonded into 3 packages. Each package contained 14 diodes as shown in Figure 9(b). The packages provide connections to several diodes in the test chamber at one time.

Current-voltage-temperature (I-V-T) data was taken using a Keithley 236 Source Measure Unit with a GPIB interface to a Macintosh running LabView. The LabView program was written by Mr. Steve Adams of WL/POOC-2. The samples being tested were secured to a copper block on top of the ceramic heater block. Prior to heating the samples, the pressure in the test chamber was reduced to $1x10^{-7}$ torr by using a turbo pump followed by an ion pump. The basic set-up is shown in Figure 10. During measurement, the temperature was progressively increased, using a MicroScience HPC1000 heater, and allowed to stabilize before taking forward and reverse current-voltage scans.

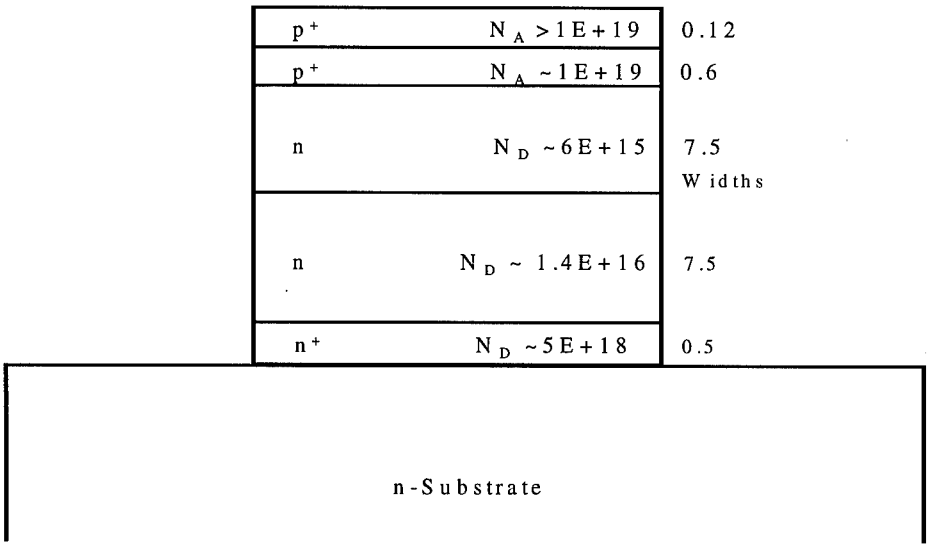

(a)

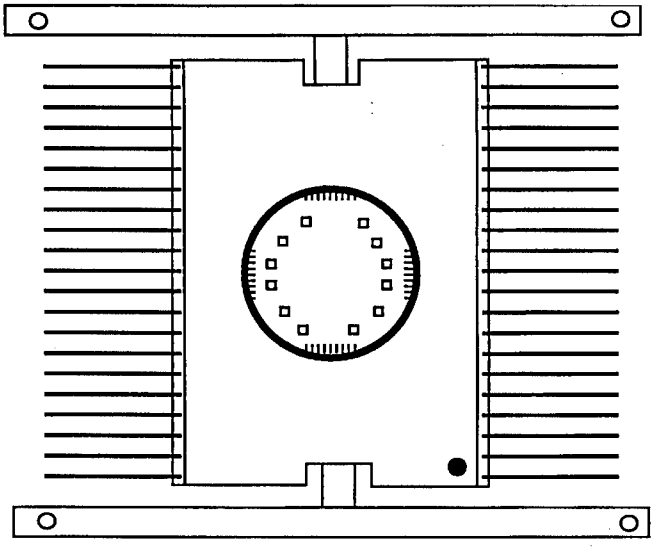

(b)

Figure 9. Diagrams of (a) 4H-SiC p^+n mesa diode structures with doping densities in cm^{-3} and widths in microns and (b) a diode package containing 14 diodes.

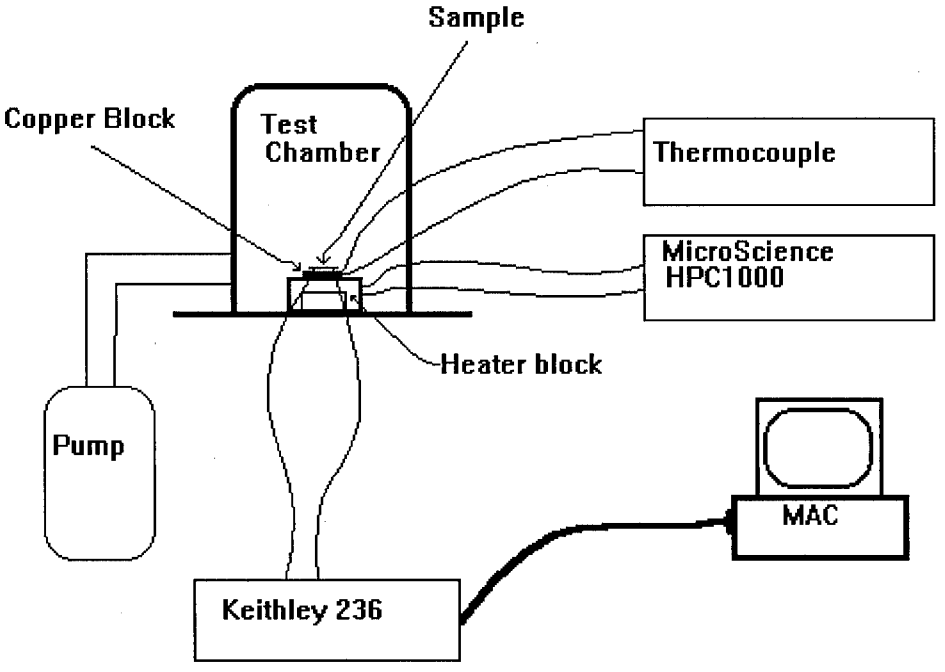

Figure 10. Experimental Set-up used for I-V-T and C-V-T measurements.

The Capacitance-voltage-temperature (C-V-T) set-up was similar to the I-V-T set-up. In place of the Keithley 236 Source Measure Unit, a Keithley 590 CV Analyzer was used. The CV Analyzer was connected to a Hewlett Packard plotter for drawing $1/C^2$ vs. V graphs. Low temperature C-V-T data was taken using AFIT's facilities. The AFIT DLTS lab has a closed cycle He refrigerator to control the temperature from 60-450 K While taking data, it was necessary to turn off all extra equipment to reduce noise in the data.

Reverse breakdown data was taken using a Tektronix 370A Programmable CurveTracer. A 100 MΩ resistor was put in series with the diode being tested in order to limit current when breakdown occurred. It was hoped that this resistor would prevent damage from occurring to the diodes being tested. Reverse breakdown data was the last experiment done so that diodes were not destroyed before other experiments could be performed. DLTS data was taken by Mr. James D. Scofield, a doctoral student at AFIT.

IV. Results and Analysis

Forward-Bias Current-Voltage-Temperature Measurements

In Figure 11, the I-V characteristics for a well-behaved diode 16 and leaky diode 17 are compared. Under forward bias, the well-behaved diode is characterized by a sharp turn-on at a relatively high "threshold" voltage, and the current is dominated by carrier diffusion in a region (d) and recombination in a region (c). The diffusion and recombination current mechanisms produce a quick rise in slope, which is a characteristic of high quality, low resistance, and efficient operation. Conversely the leaky diode conducts considerable current at much lower voltages in regions (a) and (b), which is characteristic of conduction through tunneling like leakage paths. Further, leakage currents shown exhibit a smaller slope after turn-on, which is also a characteristic of tunneling. The solid lines shown in Figure 11 are fits to the equation

$$I = I_{dif}\left[\exp\left(\frac{qV}{A_1kT}\right)-1\right]+I_{rec}\left[\exp\left(\frac{qV}{A_2kT}\right)-1\right]+I_t\exp(BV), \qquad (4.1)$$

which is very similar to Eq. (2.5). Equation (2.5) has been modified to give Eq. (4.1) by changing the current density parameter J to current I, replacing the junction voltage parameter V_D by the applied voltage V, and by replacing the shunting term V/R_{sh} with $I_o\exp(BV)$, which is a tunneling expression that gives a better fit of the leakage current. Figure 11 also shows the effect of series resistance, R_s, at voltages greater than ~2.75 V as shown in region (e). In this region, the forward voltage drop due to IR_s becomes comparable to the applied voltage. As discussed in theory, the first term of

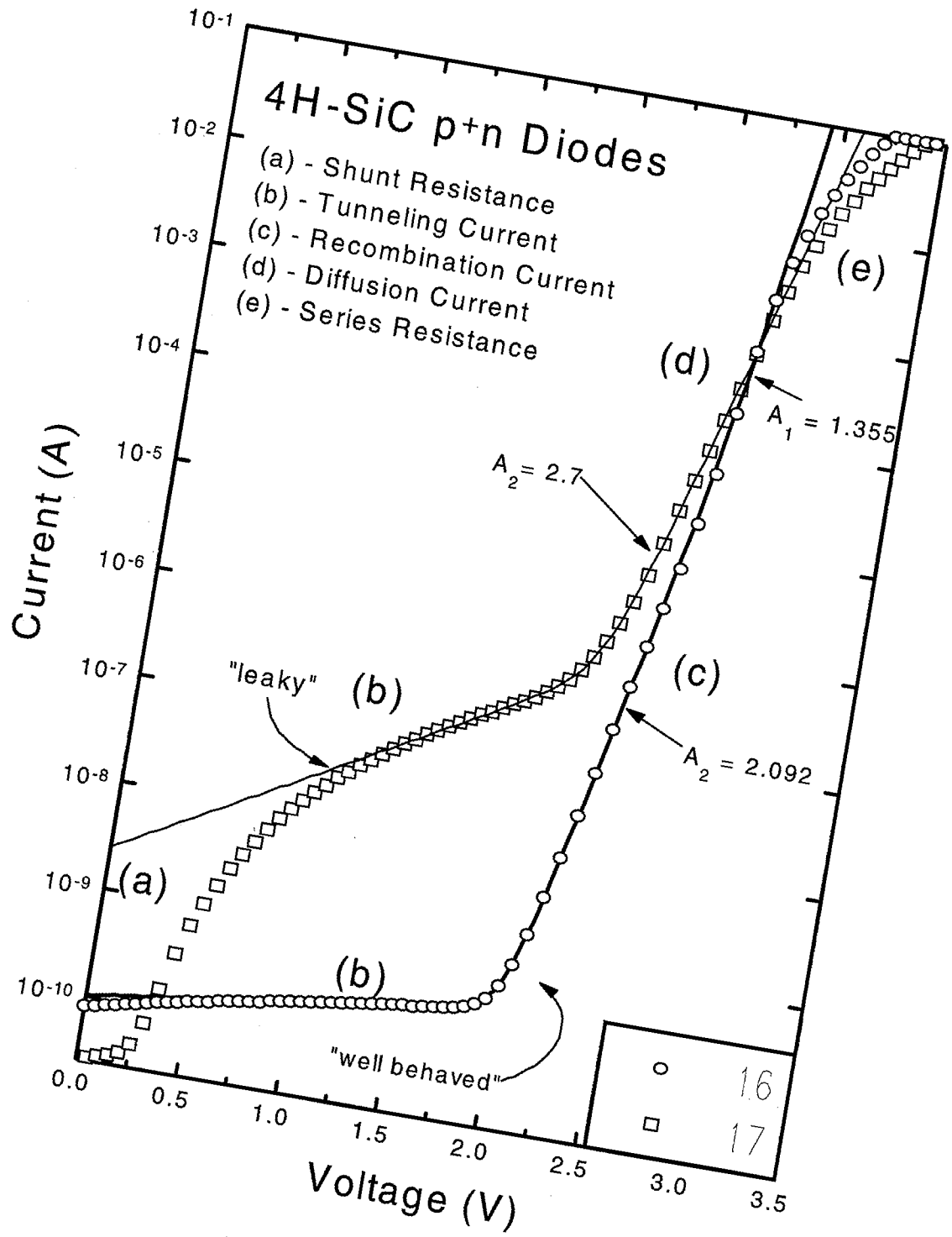

Figure 11. Forward current-voltage plot of a typical well-behaved diode 16 and a leaky diode 17.

Eq. (4.1) accounts for diffusion current, the second term for SRH recombination current, and the last term for shunt resistance leakage current due primarily to tunneling mechanisms. Recall from Eq. (2.13) and Eq. (2.30) that

$$I_{dif} \propto T^3 \exp\left(\frac{-E_g}{kT}\right), \tag{4.2}$$

and

$$I_t \propto \sqrt{\frac{1}{E_g}} V \exp\left(\frac{-8\pi\sqrt{2m^*}\,E_g^{3/2}}{3q\varepsilon_s\varepsilon_o h}\right). \tag{4.3}$$

From Eq. (2.28), the dependencies of I_{rec} on T and E_g vary as

$$I_{rec} \propto T^{5/2} \exp\left(\frac{-E_g}{2kT}\right). \tag{4.4}$$

Using Eqs. (4.1), (4.2) and (4.4), one can find the total recombination-to-diffusion current ratio and the ratio of the saturation currents, given by

$$\frac{\text{Rec.Current}}{\text{Diff.Current}} \propto \text{Exp}\left(\frac{E_g - qV}{2kT}\right), \tag{4.5}$$

and

$$\frac{I_{rec}}{I_{dif}} \propto T^{-1/2}\text{Exp}\left(\frac{E_g}{2kT}\right), \text{ respectively.} \tag{4.6}$$

From Eq. (4.5), it can be concluded that the recombination current will be more dominant for wider bandgaps, lower voltages, and lower temperatures. Conversely, diffusion current will dominate for narrower bandgap materials, higher voltages, and higher temperatures. Eqs. (4.1)-(4.4) show that both diffusion and recombination currents increase with temperature and voltage, while the tunneling current remains relatively constant. As a result, the tunneling current term should be more prominent at lower voltages and lower temperatures.

Diode 16 in Figure 11 exhibits current due to tunneling, recombination, and diffusion, while diode 17 only exhibits current due to tunneling and recombination. In agreement with the theory, the tunneling currents shown by (b) in Figure 11 dominate at low voltages, while the recombination current (c) and diffusion current (d) dominate at mid-range and high voltages, respectively. In the case of diode 16, Eq. (4.1) describes the tunneling current well over the voltage range of 0-2 V. In the range of 2-2.75 V, values of the ideality factor A_2 obtained from fits to Eq. (4.1) for six diodes ranged between 1.85 and 2.10 over temperatures of 25-250 °C. As noted earlier, a value of A_2~2 is characteristic of ideal recombination through traps at the center of the bandgap. Although it was difficult to obtain reliable values of A_1 for the well-behaved diodes using Eq. (4.1) due to series resistance effects, as shown in Figure 11 at voltages greater that ~2.75 V, typical values for A_1 ranged from ~1.3-1.4. This is indicative of current due to both diffusion and recombination processes. In the case of the leaky diode, the slope of the tunneling region (b) is very shallow, which is also consistent with theory (Reinhardt, 1994). Figure 12 shows a linear plot of I-V characteristics for diodes 16 and 17. The two diodes are nearly indistinguishable below 2.4 V. Analyzing the linear Y-axis plot provides perspective as to what the I-V curves "actually" look like. Shockley's ideal diffusion current curve has been plotted for comparison in solid line. The later but sharper turn-on of the well-behaved diode more closely matches the ideal I-V curve.

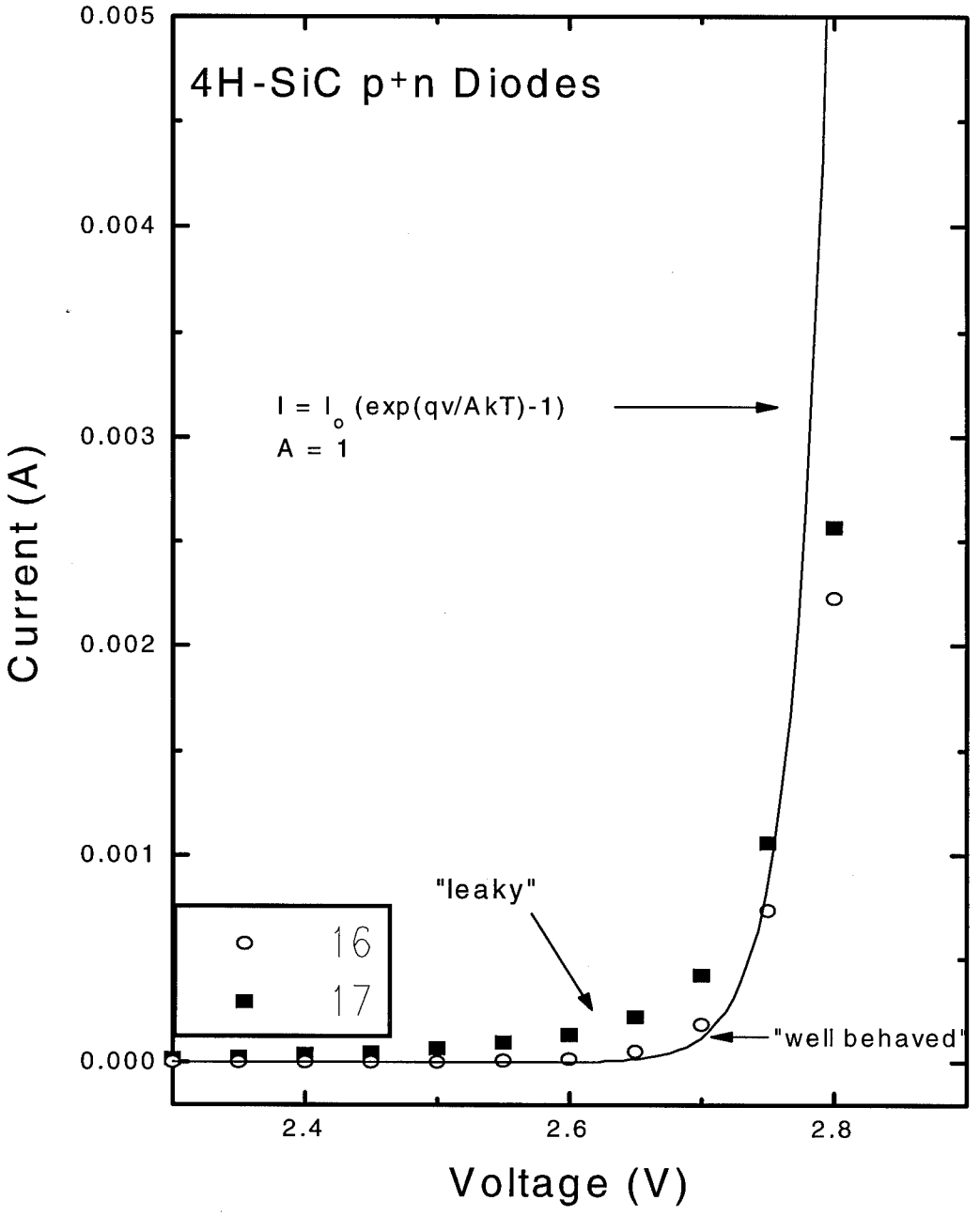

Figure 12. A linear I-V plot comparing well-behaved and the leaky diodes to Shockley's ideal diffusion model.

Forward-bias I-V characteristics measured as a function of temperature (I-V-T) for diodes 16 and 17 are shown in Figures 13 and 14, respectively. As shown in Figure 13, the voltage at which diode 16 turns on decreases with increasing temperature from ~1.9 V at 300 K to ~1.25 V at 500 K. Before the device turns on, the I-V curve is dominated by tunneling current. As predicted by Eq. (4.3), the magnitude of tunneling current is weakly dependent on temperature. After the device turns on, the forward current increases at a fixed voltage with increasing temperature. Figure 13 shows that as the temperature increases the series resistance becomes a significant factor at lower voltages. This is predicted through Eqs. (4.2) and (4.4), where at a given voltage, diffusion and recombination currents increase exponentially with temperature. In Figure 14, the effects of temperature on the I-V curves for diode 17 are compared to the room temperature I-V curve of diode 16. The leaky diode shows the same increase in recombination current and onset of series resistance at lower voltages as exhibited by the well-behaved diode. However, the tunneling currents in the leaky diode exhibit a much weaker dependence on temperature than the recombination currents. This behavior is typical of tunneling current which is weakly dependent on temperature.

Since the bandgap of 4H-SiC is 3.2 eV, the ratio of recombination-to-diffusion saturation current given by Eq. (4.6) is expected to be larger in these devices than those for similar Si and GaAs devices. Si and GaAs have bandgaps of 1.12 and 1.43 eV, respectively, and exhibit a recombination-to-diffusion saturation current ratio of 10^3 - 10^6

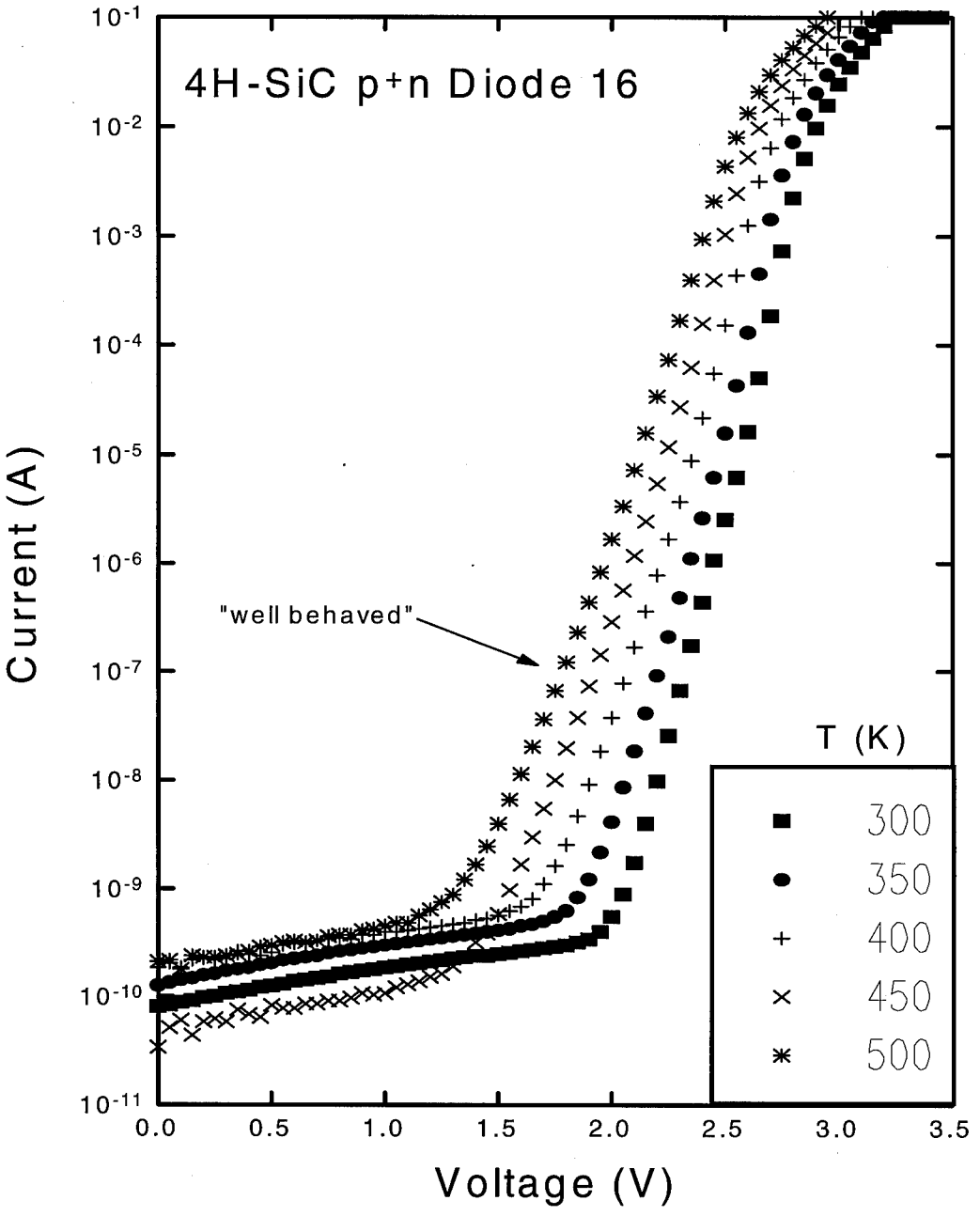

Figure 13. Forward I-V-T measurements of a typical well-behaved diode.

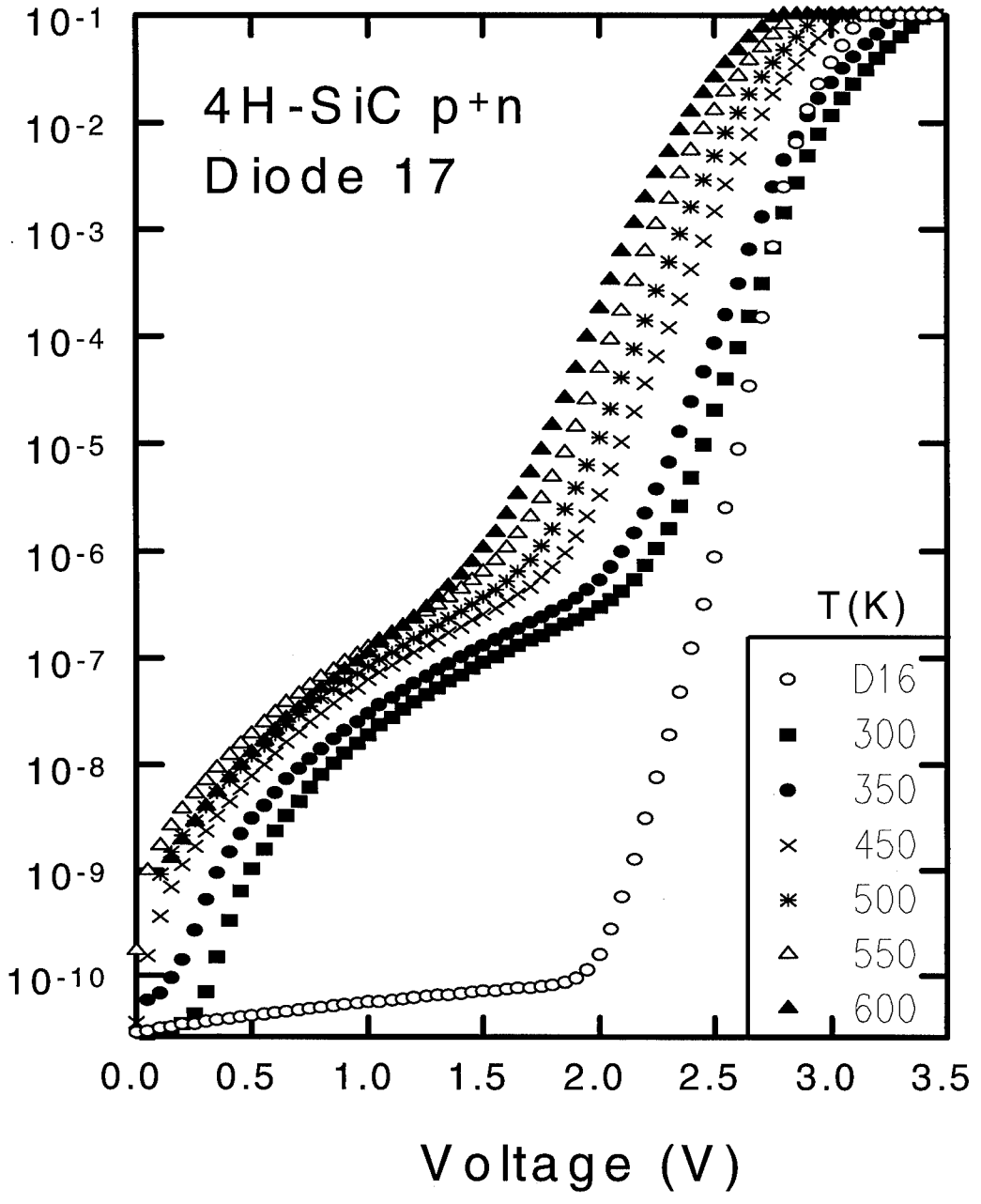

Figure 14. Forward I-V-T curves of a typical leaky diode 17 compared to a room temperature curve of a well-behaved diode 16 (o).

and 10^8 - 10^{10}, respectively. The experimental recombination-to-diffusion saturation current ratio was found for the SiC p^+n diodes by fitting the diffusion and recombination terms from Eq. (4.1). Fitting was performed on nine different well-behaved diodes, one of which is shown in Figure 15. Taking the average ratio for the nine diodes at each temperature resulted in the data shown in Figure 16. The experimental data points are compared to a theoretical solid curve calculated from Eq. (4.6). As expected the SiC ratios are much greater than that of Si or Ge, ranging from 10^{13} - 10^{28}. This ratio range is actually a low estimate of the recombination-to-diffusion ratio due to the inclusion of recombination current in the diffusion current region as indicated by the A_1 value of 1.36 in Figure 11.

The activation energy, E_A, for the $A_2 \approx 2$ recombination current for 6 well-behaved SiC p^+n diodes was calculated using Eq. (4.4), which can be rewritten in the form of

$$I_{rec} \propto T^{5/2} \exp\left(\frac{-E_a}{kT}\right). \qquad (4.4')$$

Using an Arrenhius plot, a best fit line was drawn through the $Ln(I_{rec})$ vs. 1000/T data for the diodes to yield a value for E_A as shown in Figure 17. The average value of E_A obtained was 1.56 eV, compared to a value of $E_A = E_g/2 \approx 1.6$ eV for ideal recombination current in 4H-SiC with E_g=3.2 eV.

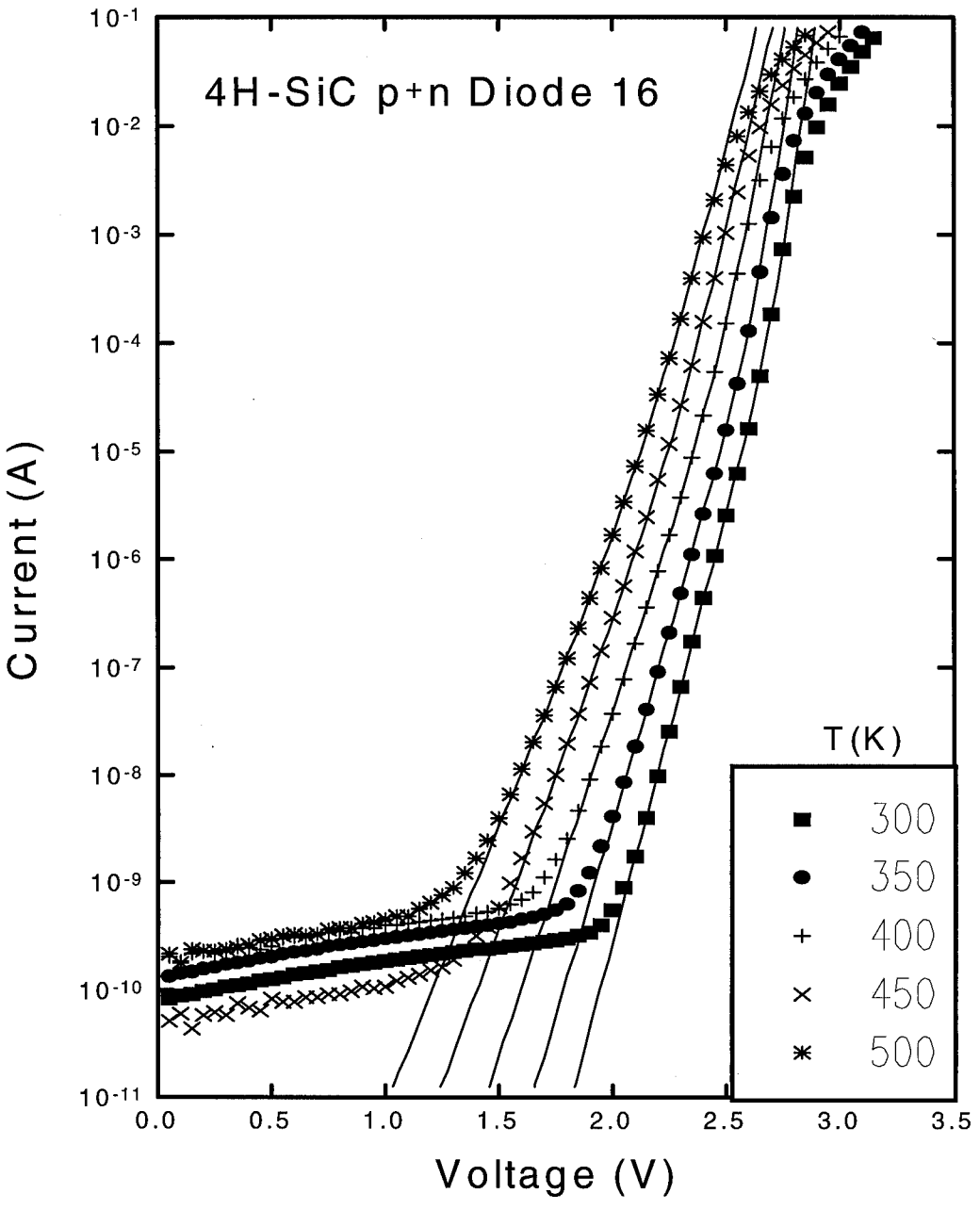

Figure 15. Forward I-V-T curves of a well-behaved diode. Experimental data is shown by symbols, while the solid lines are theoretical fits from Eq. (4.1).

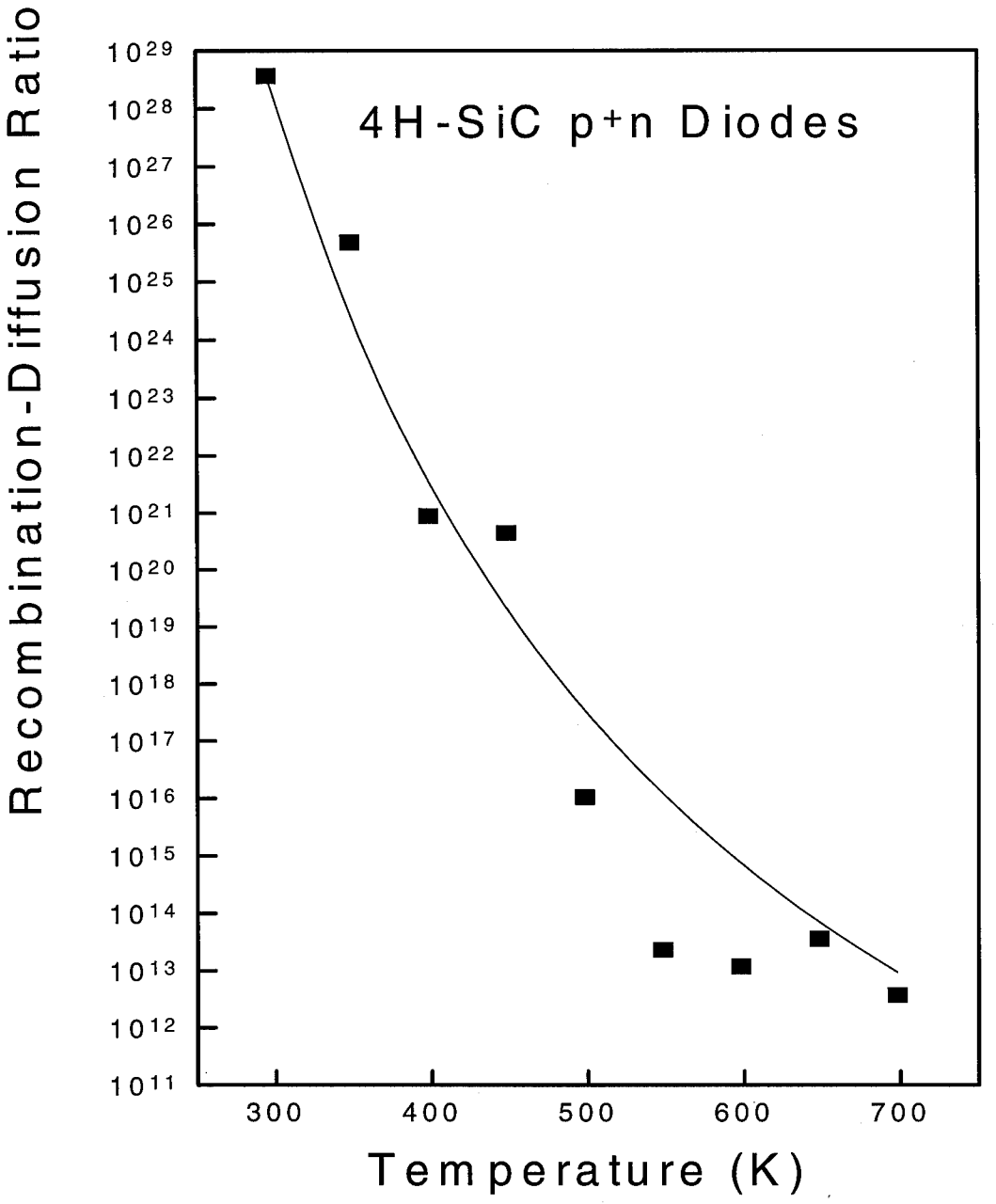

Figure 16. Comparison between the experimental recombination-diffusion current ratio and the theoretical ratio (solid line).

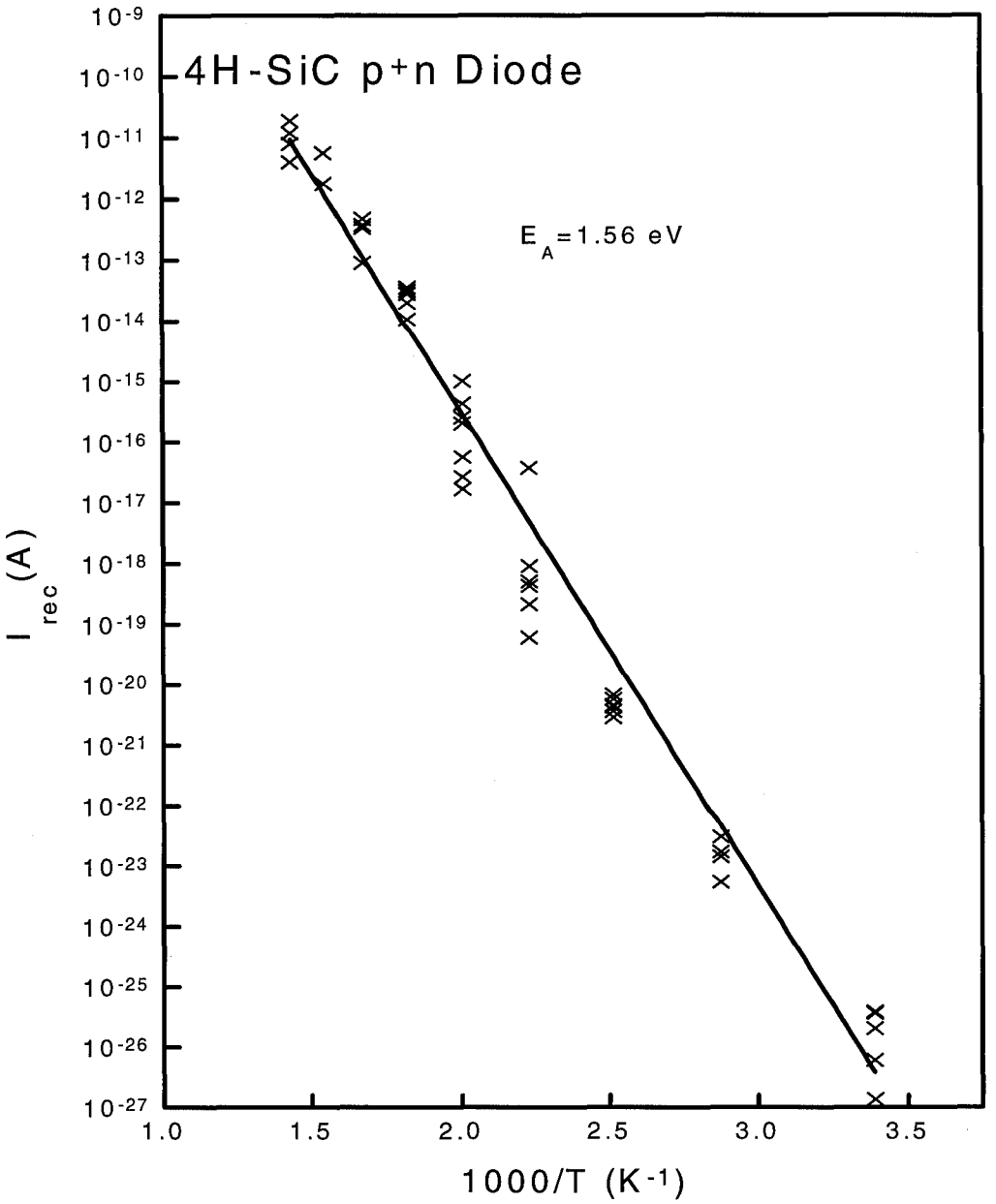

Figure 17. Plot of 6 diode's recombination currents vs. 1000/T. The average activation energy E_A = 1.56 eV has been obtained using Eq (4.4').

Reverse-Biased Current-Voltage-Temperature Measurements

A plot of reverse I-V curves for the leaky and well-behaved diodes 17 and 16, respectively, are shown in figure 18. Diode 16 exhibits reverse currents that are approximately 1000 times less than those of diode 17. The large currents of the leaky diode are due to tunneling and generation and recombination processes. The leaky diode shows an interesting feature at a reverse-bias voltage of 95 volts. At the edge of the plot, the leaky diode's current starts to rapidly increase indicating the beginning of reverse breakdown. This feature is not seen in the majority of well-behaved diode even at 120 volts. Qualitatively, this indicates breakdown due to tunneling. Some well-behaved diodes broke down suddenly at uncharacteristically low voltages due to defects. This phenomenon will be discussed in the reverse breakdown section.

Reverse I-V-T curves for diodes 13 and 17 are shown in Figures 19 and 20, respectively. As expected, the reverse currents increase with temperature due to the temperature dependence of the generation and recombination current. The activation energies of the defects through which the reverse generation and recombination current is flowing can be found by plotting the reverse current vs. 1000/T for a given voltage as shown in Figures 21 and 22, where according to Eq. (4.4') a linear slope would indicate that recombination current is flowing through one energy level. These curves are not linear on a logarithmic plot indicating the existence of tunneling current and two or more activation energy levels. Fitting Eq. (4.4') to the data from diode 18 yielded low and high temperature defect levels at 57 and 170 meV with recombination coefficients of

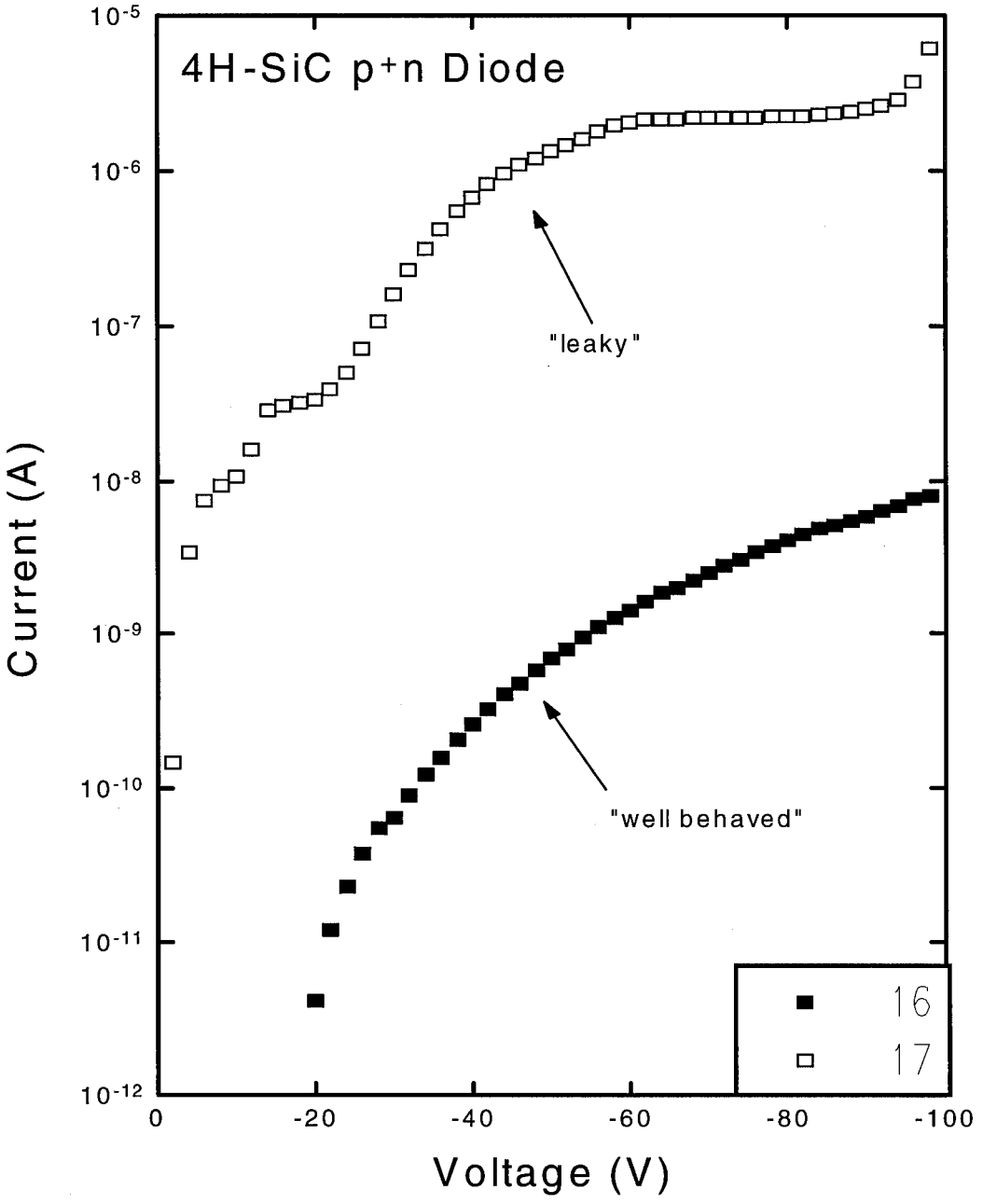

Figure 18. Reverse I-V curves of typical well-behaved and leaky diodes.

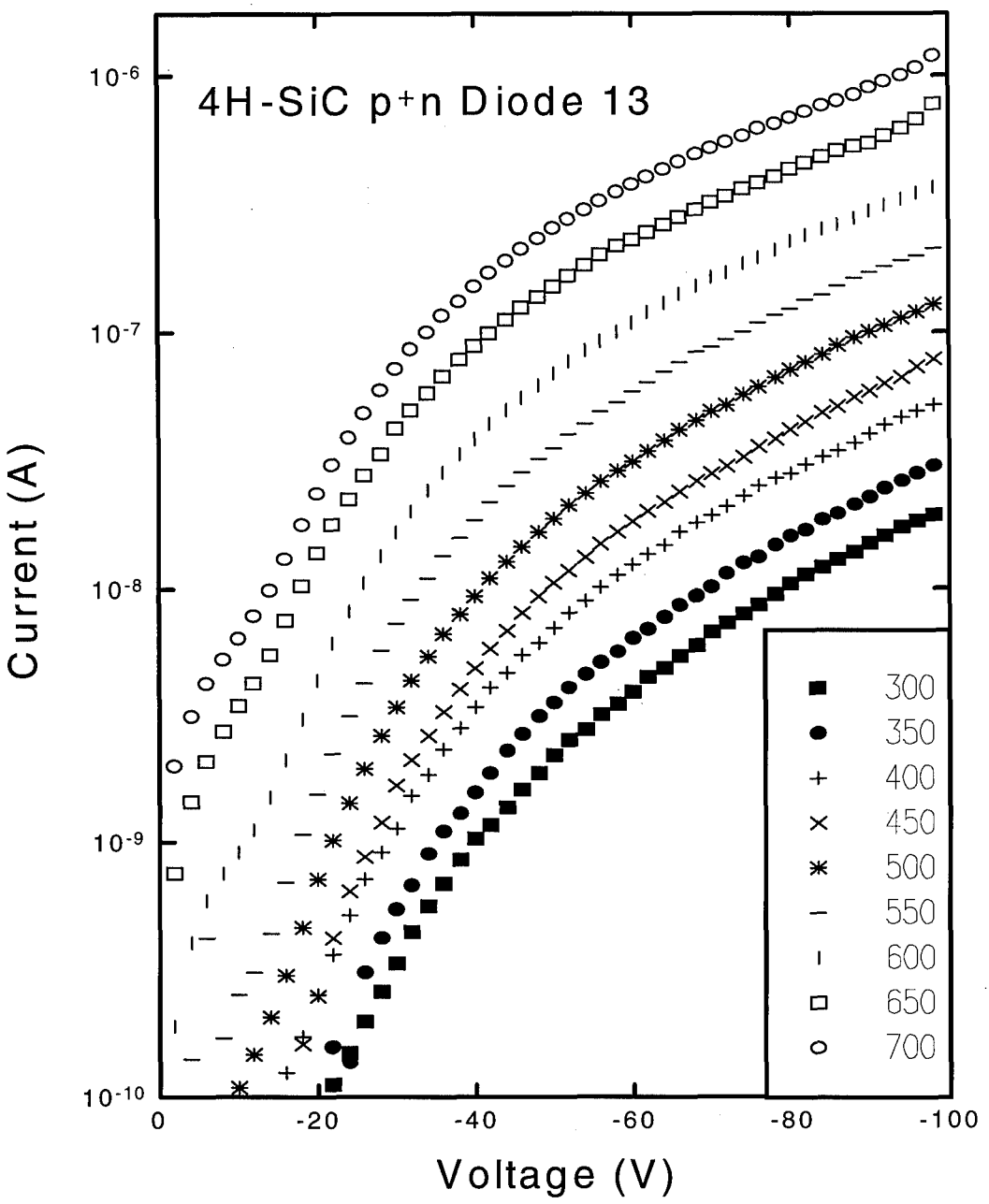

Figure 19. Reverse I-V-T curves of a well-behaved diode 13.

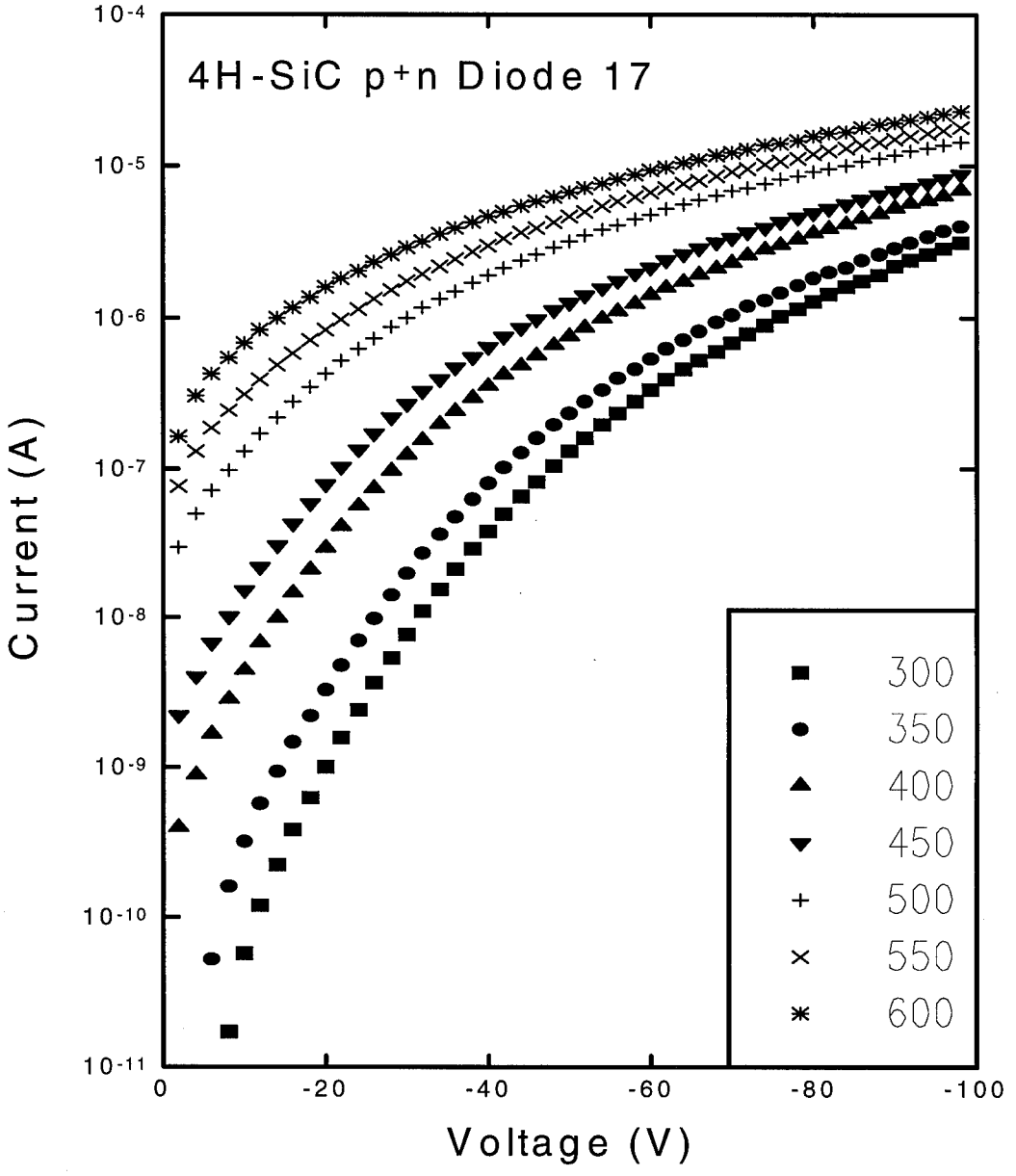

Figure 20. Reverse I-V-T curves of a typical leaky diode 17.

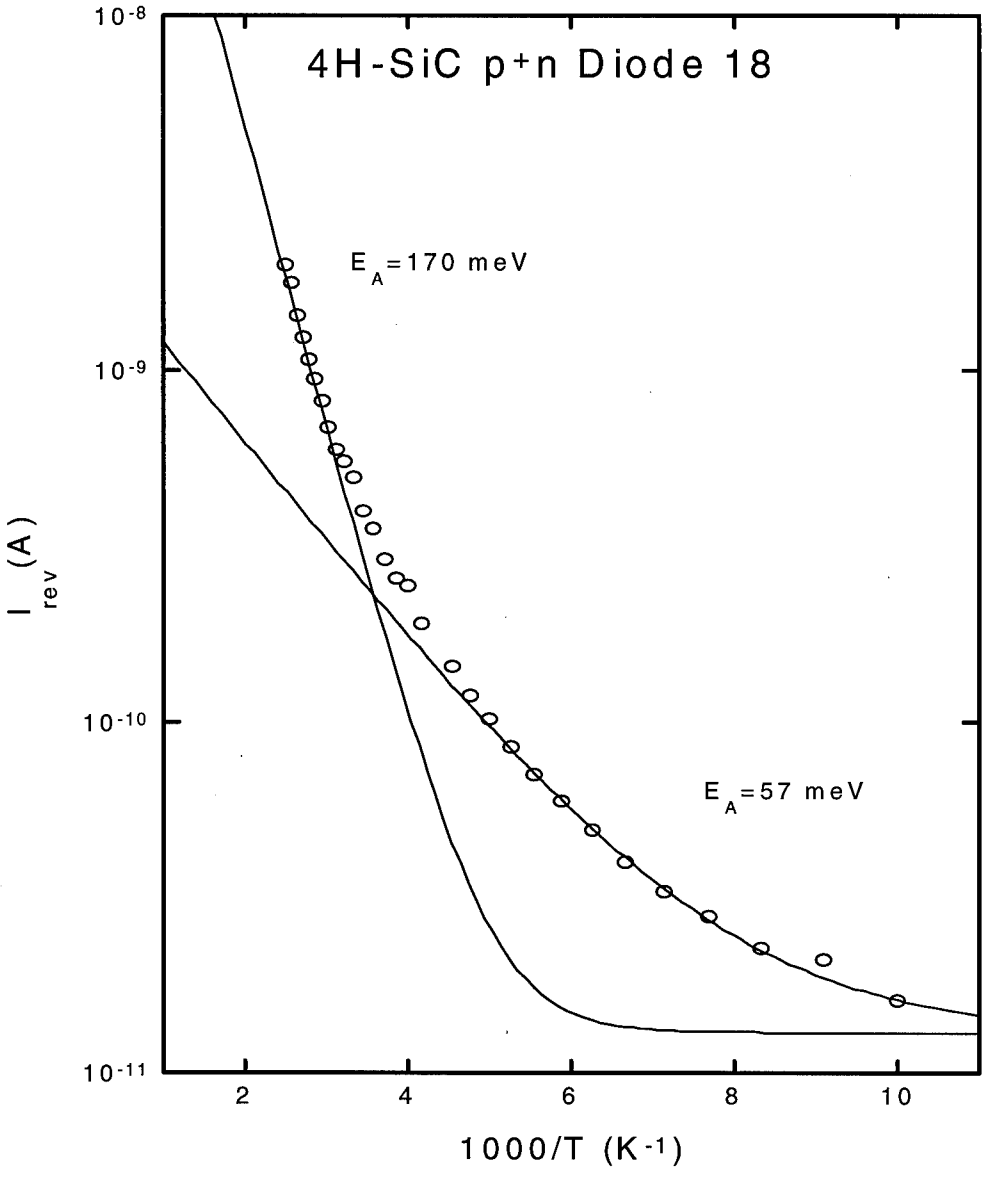

Figure 21. Plot of I_{rev} versus 1000/T. Fitting the data with Eq (4.4') gives defect levels at low and high temperatures of 57 and 170 meV, respectively.

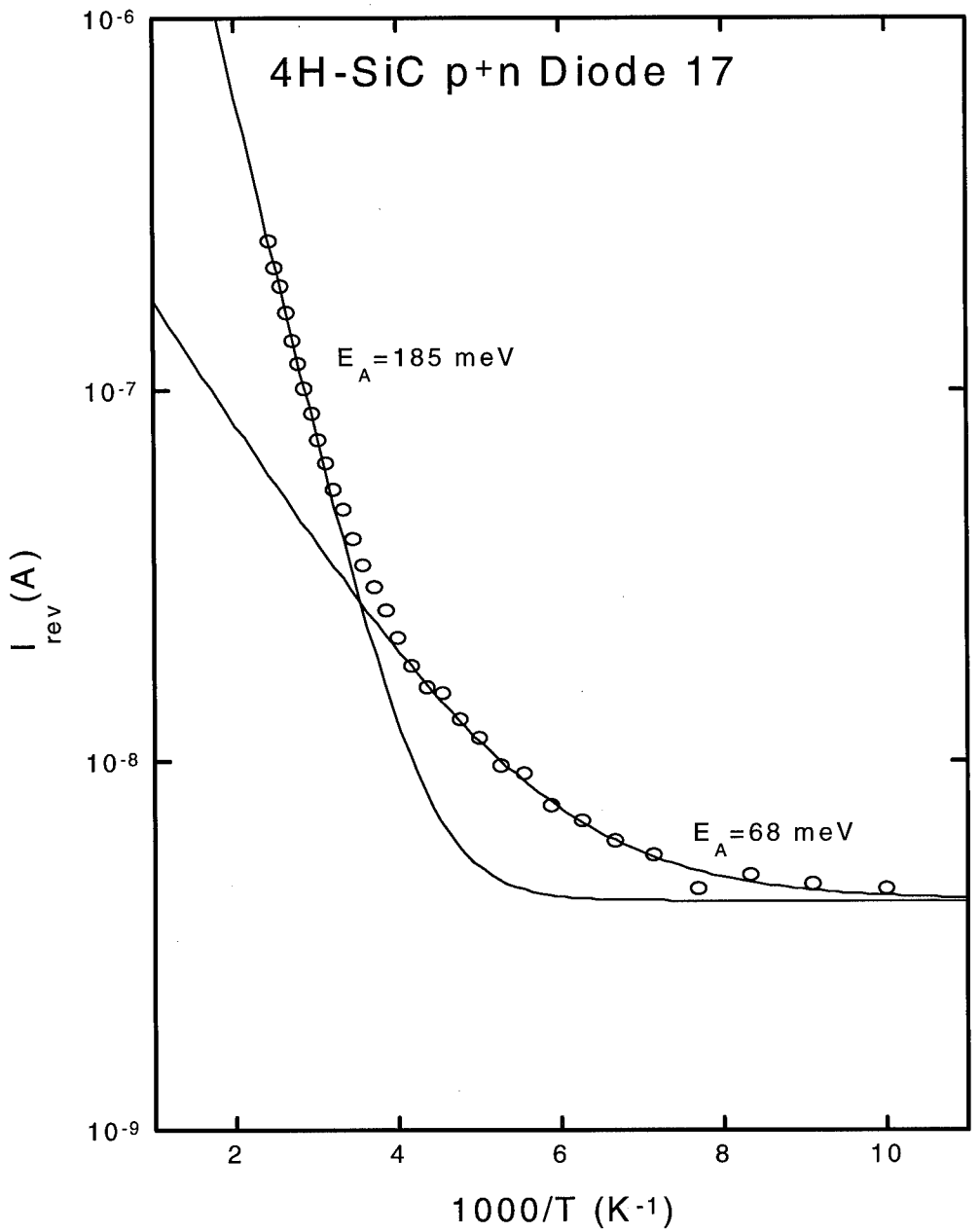

Figure 22. Plot of Irev versus 1000/T for diode 17. Modeling using Eq (4.7) gives defect levels at low and high temperature of 68 and 185 meV, respectively.

$2.3x10^{-9}$ and $2.5x10^{-7}$ Amps, respectively, and a tunneling current of $1.3x10^{-11}$ Amps. Diode 17's data yielded low and high temperature defect levels at 68 and 185 meV with coefficients $3.75x10^{-7}$ and $4.5x10^{-5}$ Amps, respectively, and a tunneling current of $4.19x10^{-9}$ Amps. The two diodes have reverse recombination energy levels that are well within experimental error of each other, yet, the leaky diode 17 had recombination coefficients and a tunneling current that are ~200 times those of diode 18. Assuming that diodes 18 and 17 have the same defect levels, as suggested by the proximity of the energy levels found in Figures 21 and 22, one can qualitatively state that the larger reverse biased tunneling and recombination currents of diode 17 are due to the greater concentration of defect levels.

Equation (4.4') was used to model reverse I-V-T data from 4 diodes on package #1 and 6 diodes on the package #2. The results are shown below in TABLE 1, where the high temperature, 300-750 K, data was taken at Wright Labs, and the low temperature, 60-400 K, data was taken at AFIT. The ± values in TABLE 1 give the range within which there is 95% confidence in calculated activation energy. In addition to uncertainty in the raw data is the modeling uncertainty due to fitting a line to a small linear portion of the plot. Given these uncertainties, the low temperature data yields two consistent activation energy levels at 55 ± 11 meV and at 173 ± 19 meV. The shallow level was obtained from the low temperature region data of diodes 3, 5, 13, 16, 17, 18, and the deeper level was obtained from the high temperature region result from diode 3 along with the low temperature values from diode 3, 5, 16, 17, 18, and 21. At high

Table 1: Activation Energy Levels Obtained by Reverse I-V-T Measurements

Package #1 Diode #	High Temp (meV)		Low Temp. (meV)	
3	161	± 98	176	± 29
			50	± 7
5	n/a		154	± 22
			36	± 14
9	230	± 31	n/a	
12	225	± 79		
			129	± 8

Package #2 Diode #	High Temp. (meV)		Low Temp. (meV)	
13	747	± 133	224	± 75
			62	± 6
16	n/a		212	± 30
			43	± 5
17	n/a		185	± 42
			68	± 33
18	n/a		170	± 24
			57	± 4
21	411	± 64	156	± 19
			67	± 10
23	968	± 212	321	± 44

temperatures, the diodes exhibited several deeper energy levels at 747, 411, and 968 meV that were reproducible for each individual diode, but were not consistently seen in other diodes.

Capacitance-Voltage-Temperature Measurements

The Keithley 590 CV Analyzer determines junction capacitance by putting a small AC voltage and a DC bias across the p-n junction diode. This varying ΔV produces a corresponding ΔQ allowing capacitance to be measured. When defect levels are present, the capacitance varies according to Eq. (2.36). Frequency induced depletion width oscillation and corresponding majority carrier oscillations into and out of the shifting depletion region alter the Fermi levels, causing the emptying and filling of defect sites according to capture and emission rates with respect to the oscillation period t. The

temperature dependent capture and emission rates and resulting temperature dependent capacitance provide a tool for the identification of defect energy levels.

An example will be used to demonstrate the change in capacitance due to the existence of a majority carrier trap. Figure 23(a) shows a p^+n diode where the junction width W varies according to Eq. (2.32), and the extent of the depletion region into each side is inversely proportional to that side's doping density as shown in Eq. (2.15). Figure 23(b) shows the energy levels within the diode under reverse bias, where E_{fn} and E_{pn} are the Fermi energy levels on the n-side and p-side of the diode, respectively, and E_t is a trap energy level. The location of the defect level in the bandgap and with respect to the Fermi levels determines the rate Eqs. (2.16)-(2.22) and hence the degree of ionization of the defect sites on each side of the semiconductor. On the p-side of the diode $E_t > E_{fp}$ and as a result, the majority of the defect electrons have recombined with majority carriers, leaving the defect sites empty. On the other hand, on the n-side $E_t < E_{fn}$, and the defect levels tend to remain filled.

In Figure 23 a full trap is depicted as having no charge, although it is common to assume this, it is not always the case. A neutrally or even negatively charged trap may have a quantum configuration allowing the capture of an electron, and likewise a neutral or positive trap can capture a hole. The main difference between the probabilities of a positive, a negative, or a neutral trap capturing an electron or a hole is in the capture cross-sections. Qualitatively one can state that due to coulombic interactions a large capture cross section will exist between an oppositely charged carrier and trap, a

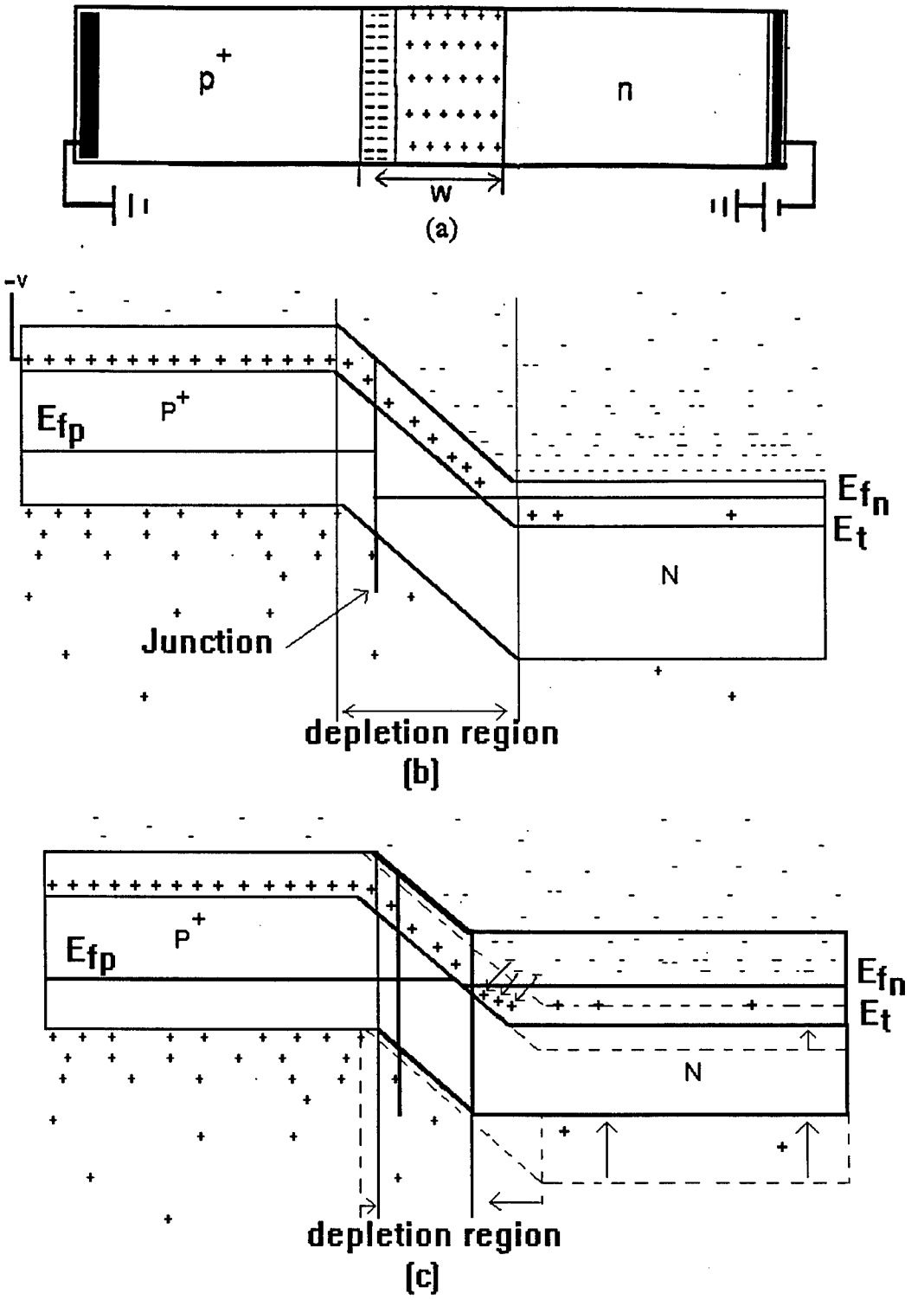

Figure 23. Illustrations of a p^+n diode where. (a) Depletion region (b) Reverse biased energy band structure with an n-side majority trap level (c) Electron capture after the elimination of the reverse bias creating a non-equilibrium condition.

mid-range capture cross section will exist between a carrier and a neutral trap, and a small cross section will exist between a carrier and a trap with the same charge. When the diode is unbiased, the junction potential decreases from that of the reversed bias, as shown in Figure 23(c). The old equilibrium is shown with dotted lines, and the new equilibrium is shown in solid lines. Notice that the depletion width has decreased slightly and that E_{fn} and has shifted so that it is slightly below E_{fp}. The depletion width change will occur primarily in the n-side of the diode due to the strong p-side doping according to Eq. (2.15). The shift of Fermi levels results in the uncovering of empty defect sites on the n-side of the semiconductor. If the capture rate is faster than the scan period, t, then these empty defect sites are quickly filled by electron capture according to Eq. (2.17), and the capacitance will be slightly less due to the cancellation of positive charge on the n-side of the diode. When the AC voltage becomes negative again, electron emission processes re-establishing the equilibrium shown in Figure 23(b).

In Figure 23(c), it was assumed that the AC frequency was much slower than the emission and capture lifetimes. This assumption is not always valid. The increase and decrease of emission and capture lifetimes with respect to the AC frequency provide a valuable analytical tool for the evaluation of capacitance data. The occurrence of a capture or emission event is dependent upon the relationship between the AC period and the event's lifetime. For simplicity, in the discussion that follows the capture or emission of holes or electrons will be referred to generically as an event. If the event lifetime is much longer than the AC period, no transitions will occur, but if the event lifetime is much shorter than the AC period, the event will occur before the AC frequency switches

re-covering (re-uncovering) the energy levels of interest. Referring back to Eqs. (2.17)-(2.22), we can see that the lifetimes are inversely proportional to thermal velocity, v_{th}, which is proportional to temperature.

A hypothetical case will illustrate how the changing of event lifetimes with respect to the AC voltage can be used to identify defect sites. The CV Analyzer allows measurement of capacitance readings with a 100 kHz and 1 MHz scan rate. Given an event lifetime of longer than the AC period, the event can not occur. As temperature is increased the event lifetime approaches the AC period, producing a change in capacitance due to some capture or emission events occurring. When the temperature reaches a point such that the two lifetimes are equal, then roughly half the events will occur with each π shift of the AC cycle, and dC/dT will be at a maximum or minimum. As temperature continues to increase, all of the trap sites will participate in the event. The 1 MHz scan will be similar to the 100 kHz scan except that it will take a greater temperature for the event lifetime to be fast enough to occur with the 1 MHz scan. The result is that the capacitance vs. temperature slope shift will occur at higher temperatures for the 1 MHz scan.

The capacitance data presented in Figure 24 are from diodes 16, 17 and 18 located on the second package. The data were taken at bias voltages of 0, -10, and -20 volts with a 1 MHz scan rate. The most prominent feature of the plot is the large increase of capacitance occurring at temperatures between 60 and 120 K. This large step in capacitance is due to the freeze-out of carriers at low temperature, which was depicted in Figure 3. At very low temperatures, the dopants, according to Fermi statistics, do not

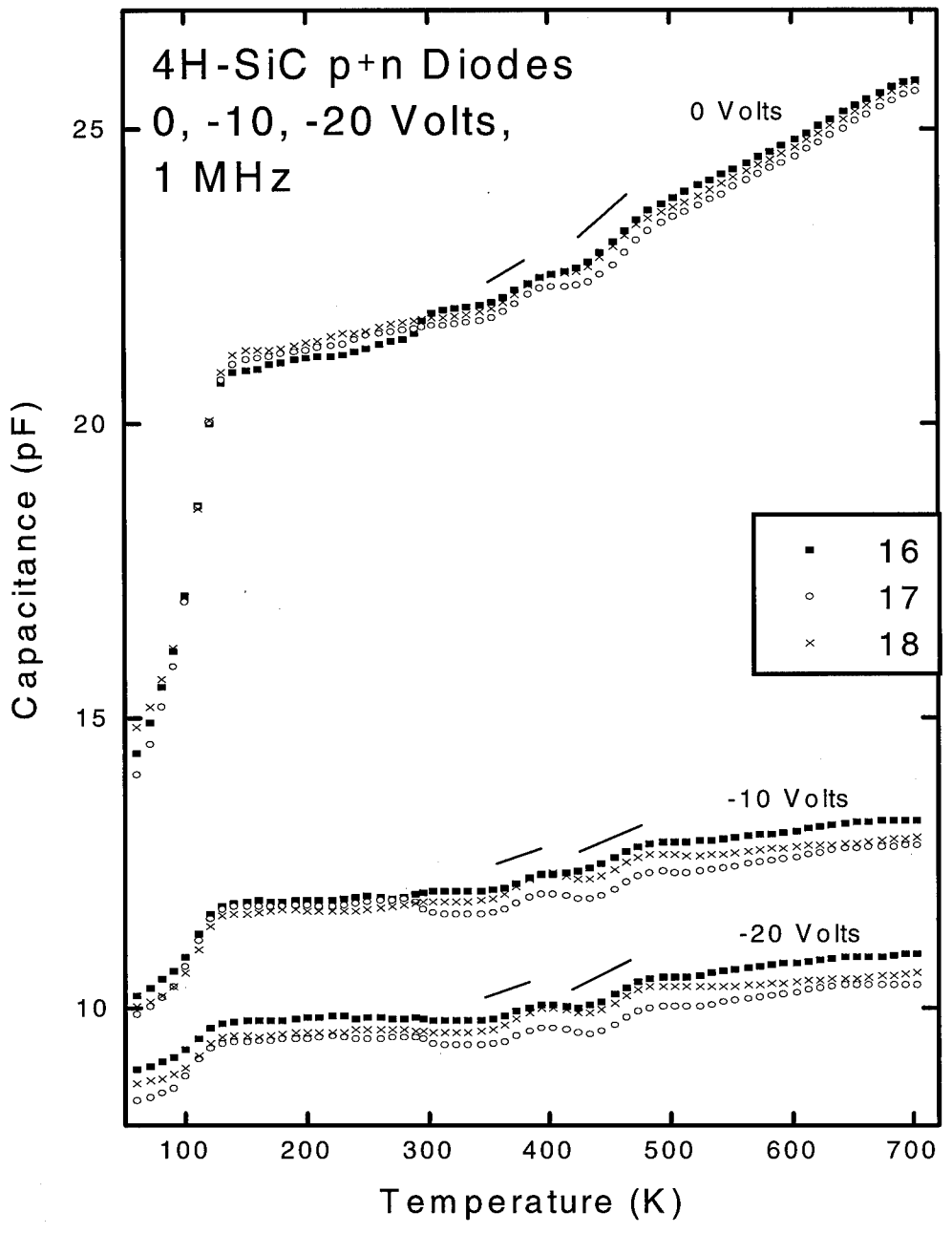

Figure 24. Capacitance vs. temperature plot of diodes 16, 17, and 18 biased by 0, -10, and -20 volts with a 1 MHz scan rate.

become ionized, and the SCL does not exist. As the temperature is increased a large increase in capacitance occurs due to emission limited trapping. On the n-side, the oscillation frequency ω is approximately equal to the dopant's electron emission rate, e_n, but is faster than the dopant's electron capture rate, c_n, due to the lack of free carriers. This causes the capacitance to increase rapidly with temperature as the emission rate equals and exceeds the oscillation frequency. Above 120 K, the donor sites are ionized, and left uncompensated near the junction forming the SCL.

The 100 kHz and 1 MHz data taken for diode 18 are compared in Figure 25. As expected, the freeze out occurs at the same temperature for each of the three voltage measurements. Taking the derivatives with respect to temperature allows one to find the maximum rate of change of capacitance with respect to temperature. These peaks and troughs will correspond to the emission lifetimes of the majority and minority carrier traps, respectively, or conversely, to the capture lifetime of minority or majority carrier traps, respectively. The derivative of Figure 25 has been taken and is shown in Figure 26. As expected, the low temperature 100 kHz maxima occurs at a lower temperature than that of the 1 MHz maxima.

Since the emission rate increases with temperature as $e_p \propto \exp(-E_a/kT)$ (Lang, 1974:3023), the activation energy E_a can be determined by setting $e_p=\omega(\Delta V_{ac})$. Taking the ratio of the two scan frequencies, f_1 and f_2, and the corresponding temperature maxima yields (Tan and Xu, 1989:28)

$$E_a = \frac{kT_1T_2}{T_2 - T_1}\left[\exp\left(\frac{f_1}{f_2}\right) - 2\ln\left(\frac{T_2}{T_1}\right)\right], \qquad (4.8)$$

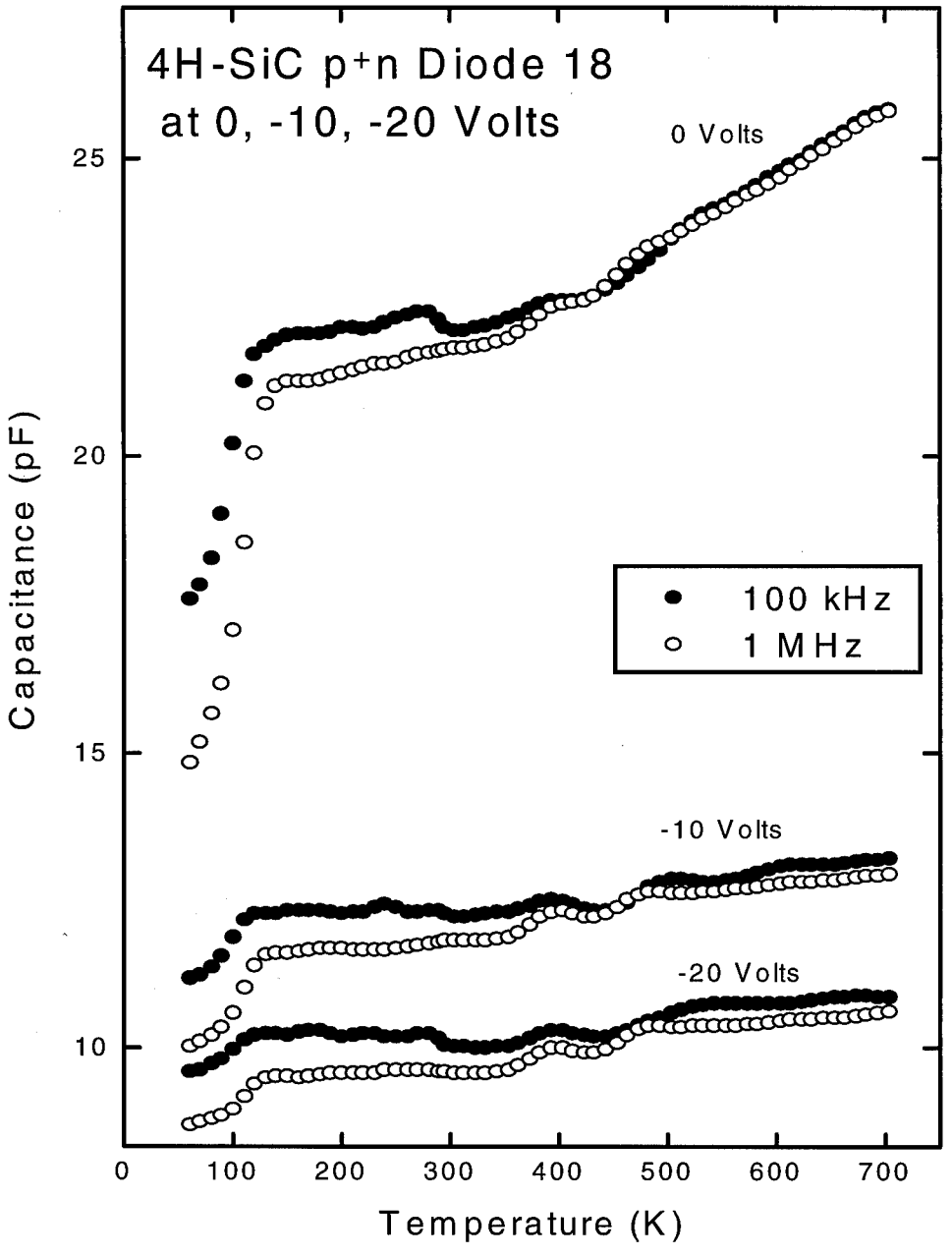

Figure 25. 100 kHz and 1 MHz capacitance vs. temperature plot of diode 18 taken at biases of 0, -10, and -20 volts.

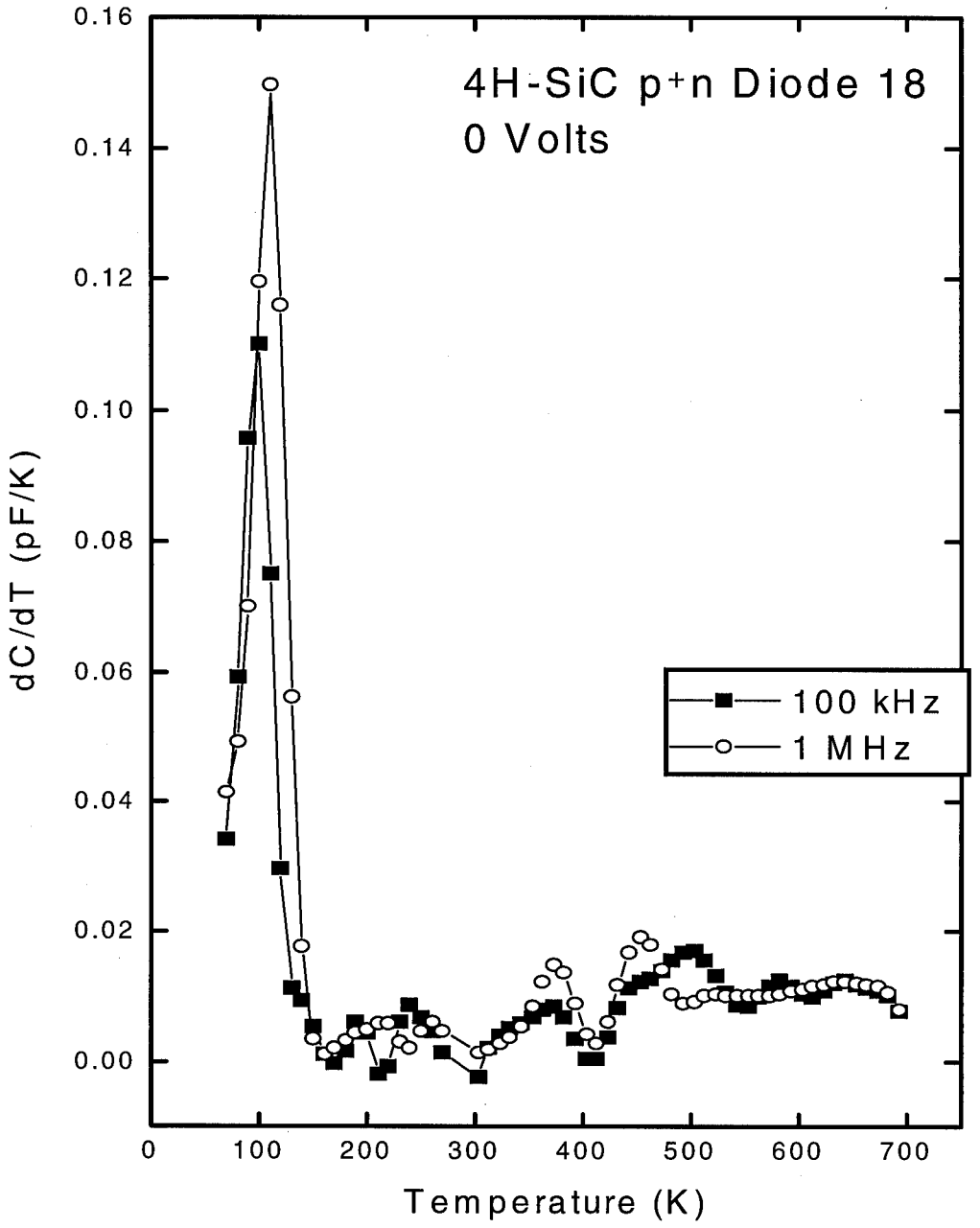

Figure 26. Plot of dC/dT vs. temperature from the 0 voltage data used in Figure 25.

where it has been assumed that $T_2 - T_1 << T_1$ or T_2. Averaging T_2 and T_1 from the nine data sets (three diodes at three voltages) gives $T_1 = 96.25 \pm 3.29$ K and $T_2 = 107.78 \pm 1.47$ K yielding an activation energy of 70 ± 20 meV. This result agrees moderately well with the reverse current result of 55 ± 11 meV.

Referring to Figures 25 and 26, it can be seen that the 100 kHz peaks and valleys lead the 1 MHz peaks and valleys. The many peaks and valleys indicate that there are several different defect sites, but do not yield a plausible activation energy for these defect levels. Results were similar for all three diodes at each of the three voltages.

The general trend of the capacitance data presented in Figure 24 can be verified by comparing them to the theoretical model shown in figure 27. The theoretical model has been calculated using Eqs. (2.1), (2.33), (2.34), the diode doping densities depicted in Figure 9(a), and the density of states in the conduction and valence bands discussed on page 9. The experimental data and the theoretical model correspond nicely to each other, although the experimental data shows a slightly higher capacitance for each bias, and a greater temperature dependence. The trends of both the experimental data and the theoretical model can be qualitatively explained by simplifying Equation (2.34) to yield

$$C \propto \sqrt{\frac{1}{V_{bi} - V - 2kT/q}}. \tag{4.9}$$

This shows that as the applied voltage V becomes more negative, the temperature term becomes negligible, while at small voltages, the capacitance has a greater temperature dependence. This qualitative analysis is confirmed by both the experimental and

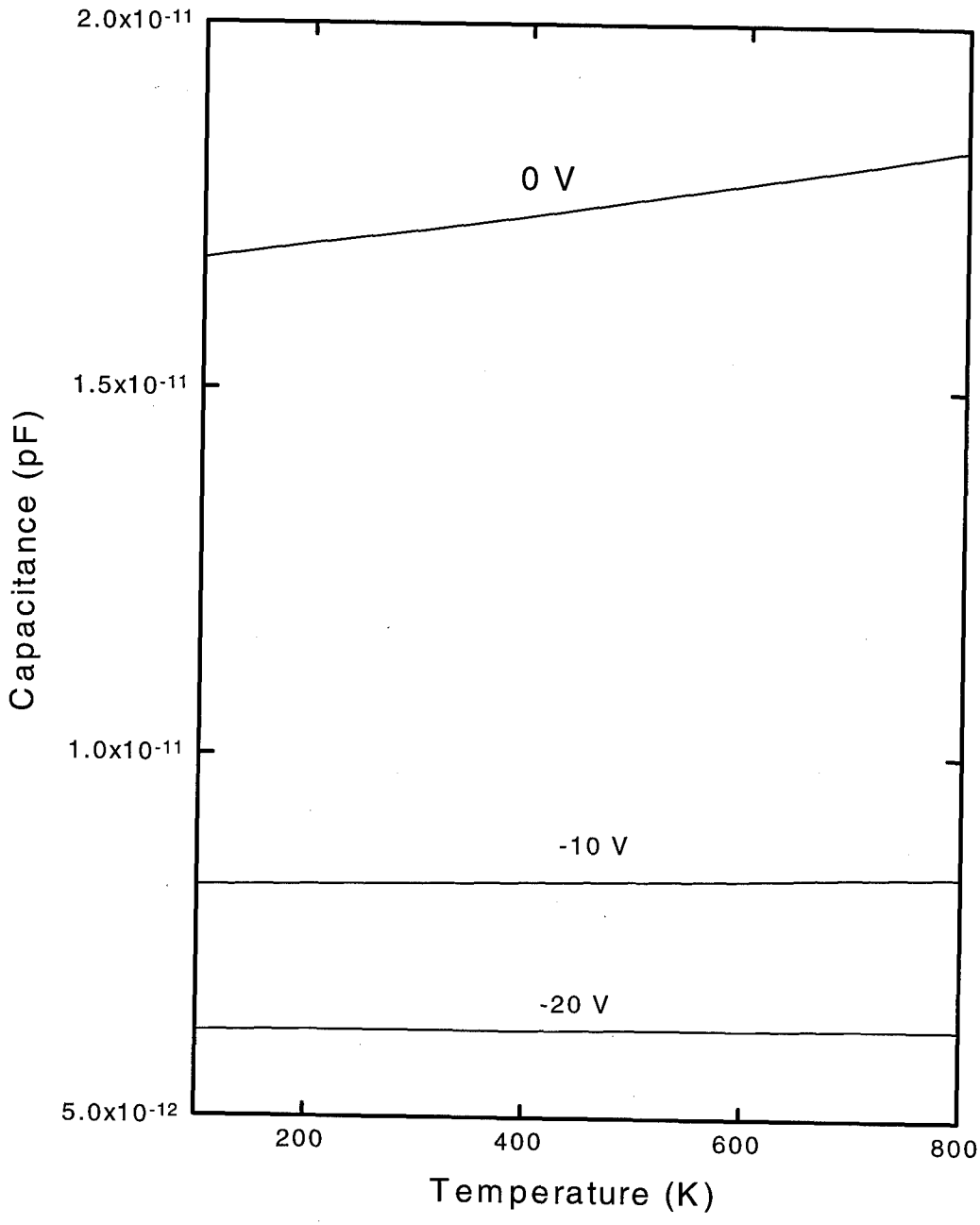

Figure 27. Theoretical results of capacitance vs. temperature for a 4H-SiC p^+n diode biased at 0, -10, and -20 volts for the top, middle, and bottom line, respectively.

theoretical data, where the top curves at 0 volt have a stronger temperature dependence than those at -10 and -20 volts.

An interesting feature of Figure 24 is the capacitance curves of each diode with respect to each other. At each of the three voltages and over the majority of the temperature range, diode 16 has the highest capacitance value, followed by diode 18 and finally diode 17. Assuming the diodes have identical built-in voltages, surface areas, and defect levels, this systematic difference in capacitance can be attributed to one of two things. The lower capacitance of a diode can be attributed to a greater or lower n-side concentration of majority or minority carrier traps, respectively. A greater concentration of majority carrier traps produces a smaller increase in $+\Delta Q$ for a given $+\Delta V$ due to a greater number of electrons been captured, and a lower concentration of minority carrier traps produces a smaller (in absolute value) $-\Delta Q$ for a given $-\Delta V$ due to the smaller number of holes emitted. Qualitatively, one can distinguish whether these are majority or minority carrier traps by examining the forward and reverse I-V curves of the diodes shown in Figures 28 and 29, respectively.

The figures show that diode 17 is the leakiest diode, diode 18 is well-behaved, and well-behaved diode 16 has the least amount of recombination and tunneling current under forward bias, and generation and tunneling current under reverse bias. As suggested by the reverse I-V results shown in TABLE 1, the diodes may have the same defect energy levels. One can speculate that diode 17 has the greatest number of defects, as indicated by the highest tunneling current, followed by 18 and 16. If diode 17 has the greatest number of defects and the lowest capacitance, then it stands to reason that the defect levels are majority carrier traps.

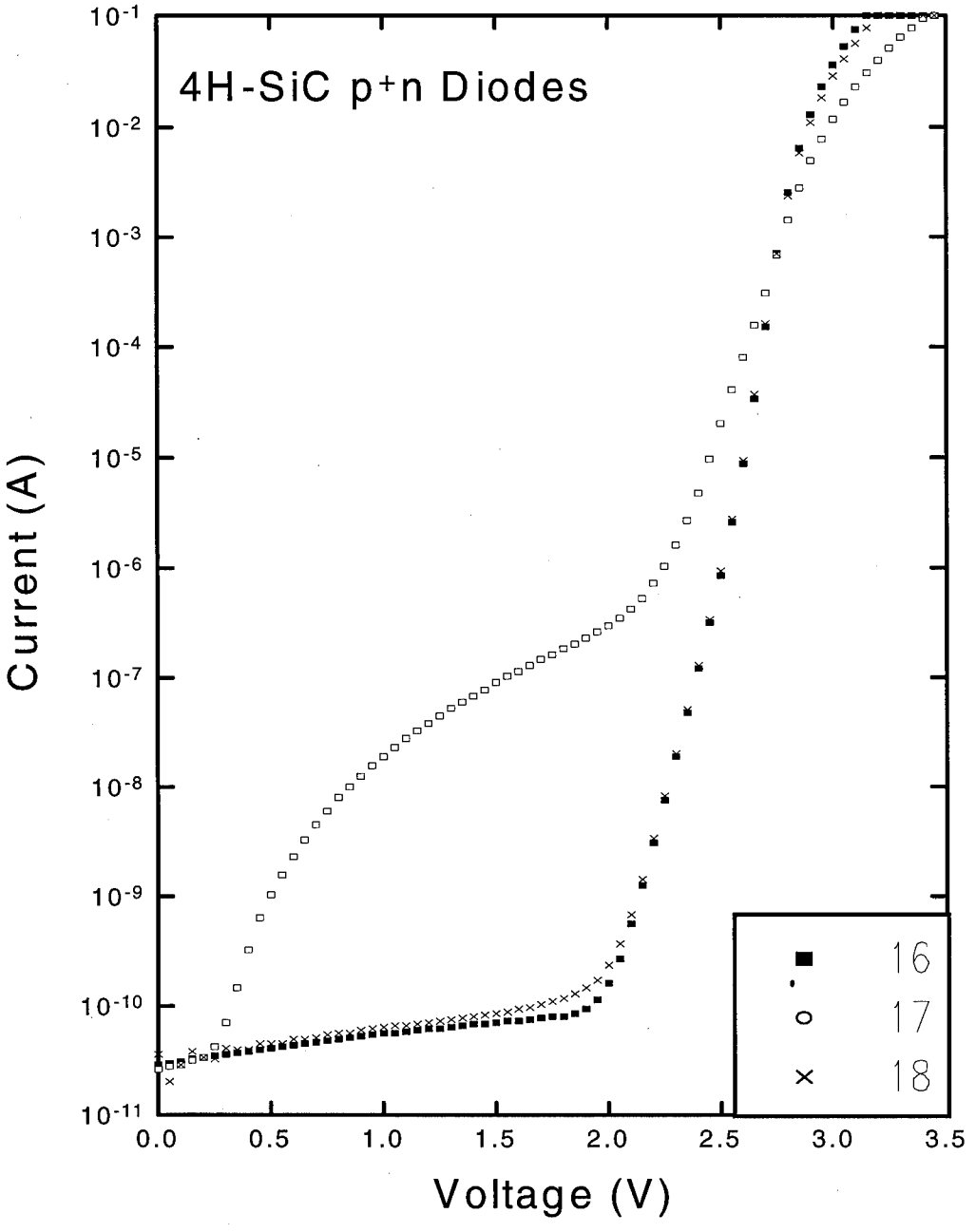

Figure 28. Forward I-V data for diodes 16, 17, and 18.

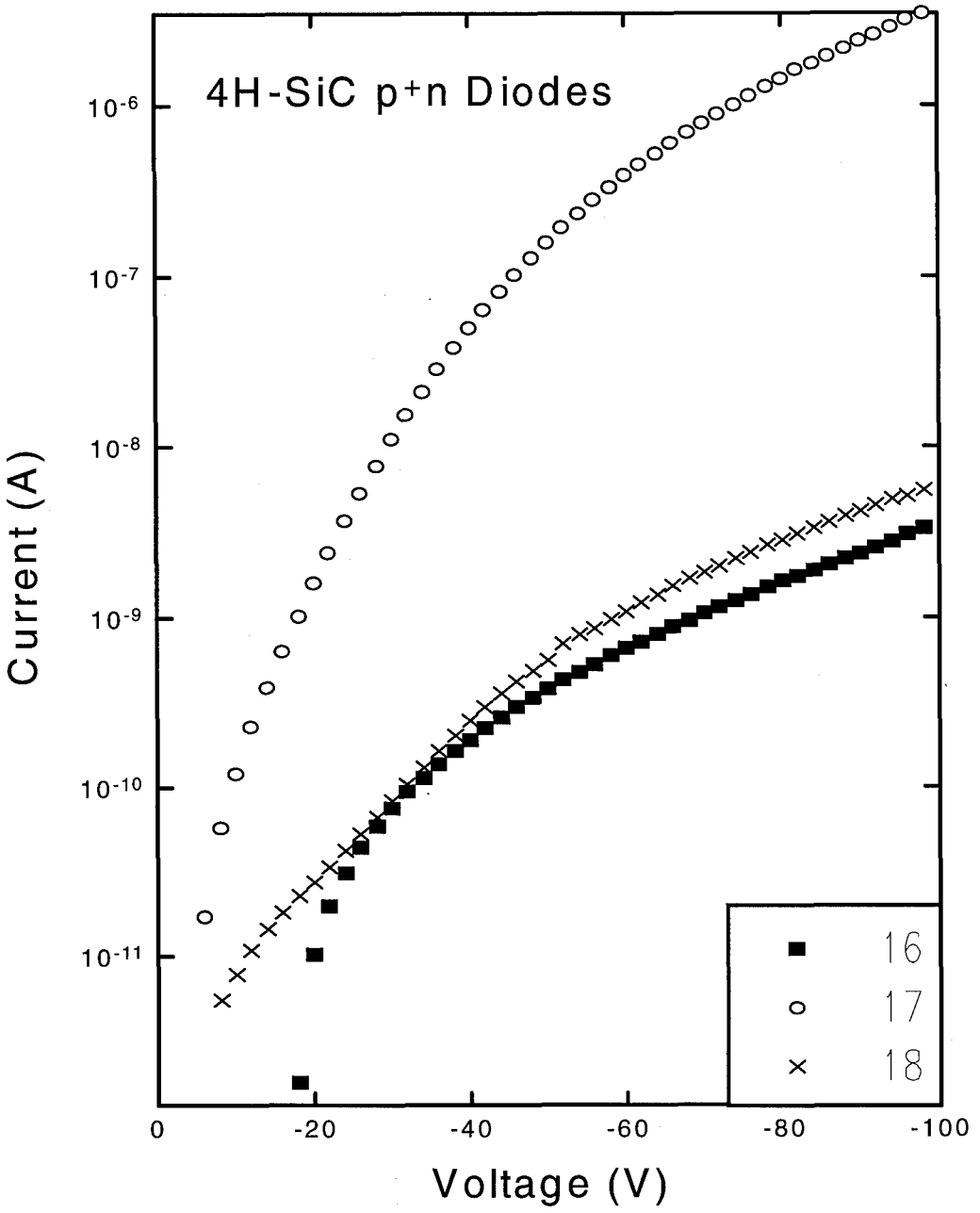

Figure 29. Reverse I-V data for diodes 16, 17, and 18.

Capacitance vs. voltage data was taken with the Keithley 290 CV analyzer and the data was plotted as $1/C^2$ vs. V on a plotter. $1/C^2$ vs. V data can be used to experimentally determine the doping density. Squaring Eq. (2.34) and taking the inverse gives

$$\frac{1}{C^2} = bV + b\left(V_{bi} - \frac{2kT}{q}\right), \tag{4.10}$$

where

$$b = \frac{-2}{S^2 q \varepsilon_s N_D} \tag{4.11}$$

is the slope of a line. $1/C^2$ vs. V data was taken for diodes 16, 17, and 18 at 1 MHz and 100 kHz for temperatures from 22 to 430 °C in ten degree increments over a voltage range of -20 through 2 volts. Taking the differential slope and calculating the doping density produce the density profiles shown in Figures 30 and 31. These plots show doping density profiles ranging from $4x10^{15}$ to $1x10^{16}$ cm^{-3} at applied voltages of zero to -20 volts, respectively. This agrees well with Cree's specified doping densities shown in Figure 9(a), where the n-side doping density increases from $6x10^{15}$ cm^{-3}, near the junction, to $1x10^{16}$ at 7.5 microns from the junction. The low doping density values seen in Figures 30 and 31 for the 100 kHz scans rate is consistent with pervious conclusions regarding the existence of defect or impurity majority carrier traps on the n-side of the diode. At the slower scan rate of 100 kHz more n-side majority carrier traps are able to participate in capture and emission events, which according to Eq. (2.36) makes the doping densities appear lower.

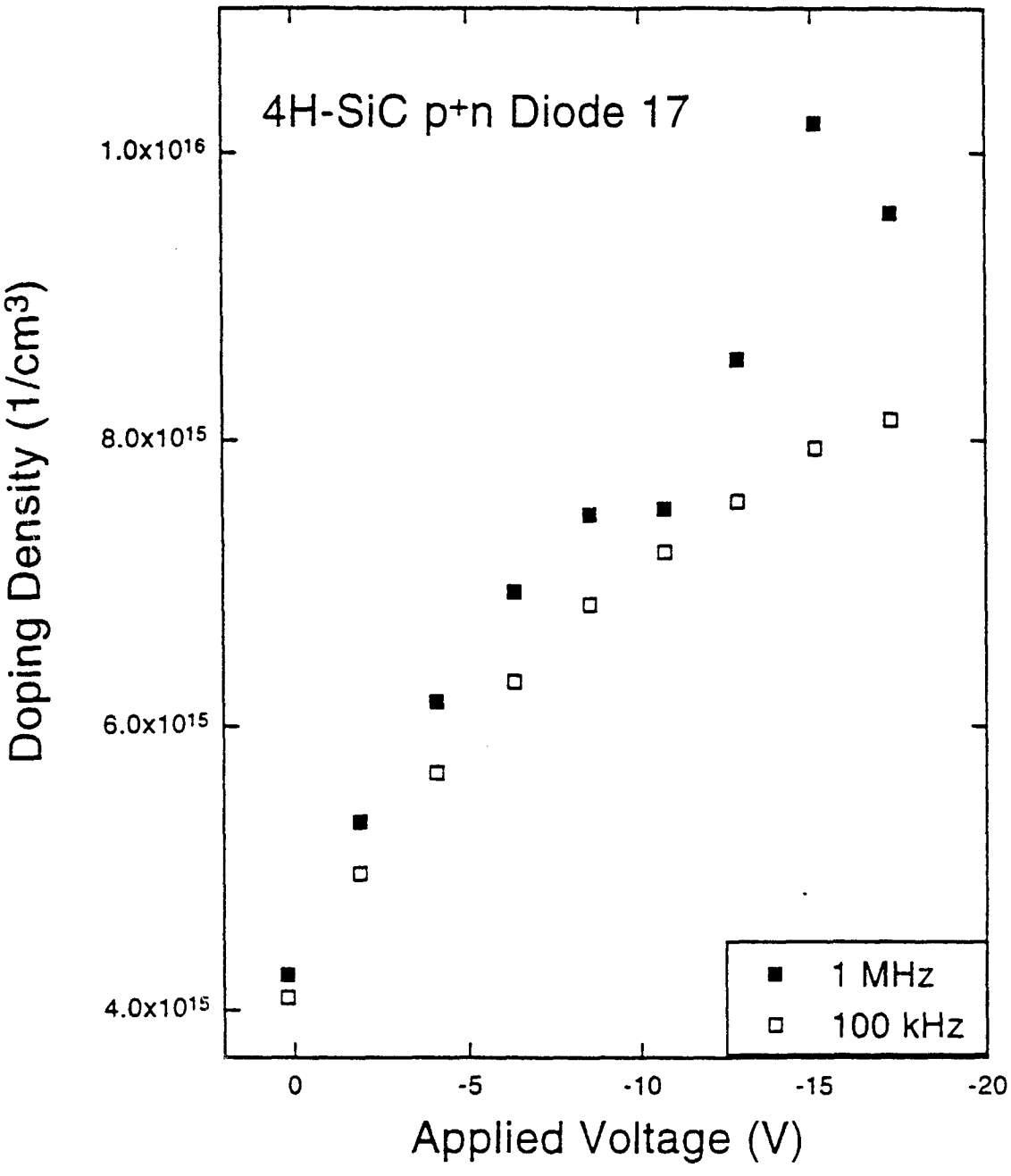

Figure 30. Doping density profiles of diode 17 calculated by taking the derivative of $1/C^2$ vs. V.

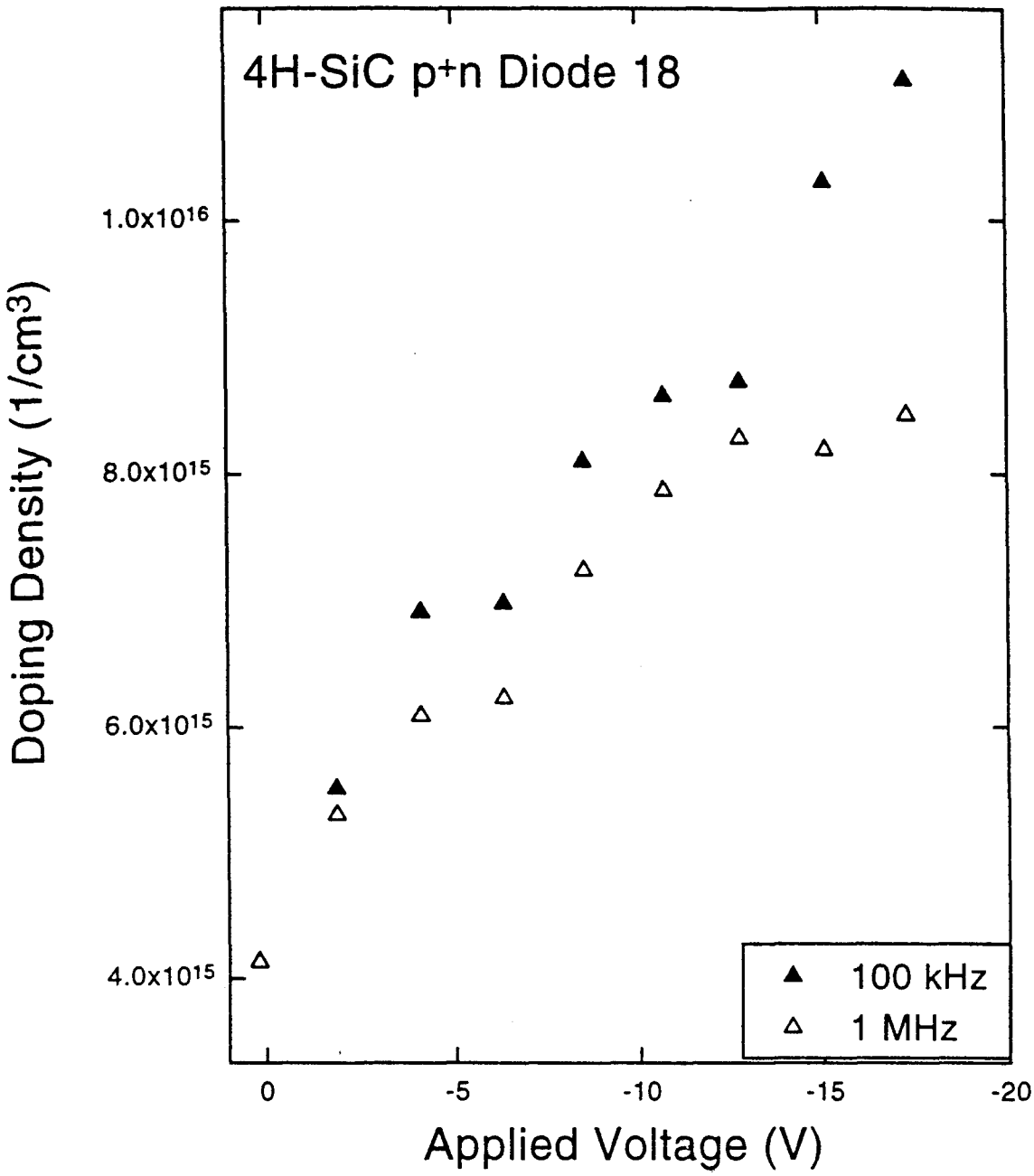

Figure 31. Doping density profiles of diode 18 calculated by taking the derivative of $1/C^2$ vs. V.

Deep Level Transient Spectroscopy Measurements

The DLTS method for characterizing trap levels is a valuable technique, allowing one to determining trap activation energies, cross sections, and concentrations. DLTS data are collected by varying temperature and measuring the junction capacitance transients that result from applied voltage pulse induced non-equilibrium carrier concentrations. A forward voltage V_1 is applied long enough for the device to reach equilibrium as dictated by capture and emission processes shown in Eqs. (2.17)-(2.22). At t=0, a negative voltage pulse, V_2, is applied. As discussed in the previous section, V_2 creates a non-equilibrium condition due to the drift of free carriers away from the junction and corresponding shift of the Fermi levels. At t=0, the lack of free carriers in the vicinity of defect sites, located in the newly created depletion region, results in emission dominated transitions, and subsequently a positive or negative capacitance transient for majority or minority traps, respectively. The capacitance of the transient is measured at two times, t_1 and t_2. Graphing the capacitance at t_1 minus the capacitance at t_2 vs. temperature, $[C(t_1) - C(t_2)]$ vs. T, allows one to view the rate of change of capacitance, called the DLTS signal, with respect to temperature as illustrated in Figure 32.

Of the 10 diodes analyzed using DLTS techniques, 5 exhibited what is suspected to be the same trap energy level at the value of 150 ± 34 meV. This is consistent with the reverse I-V-T determined level at 173 ± 19 meV. The DLTS results from 3 of the diodes yielded various deeper level traps having concentrations on the order of $0.001\ N_D$. The reverse I-V-T technique for determining trap energy levels is not able to see these deeper

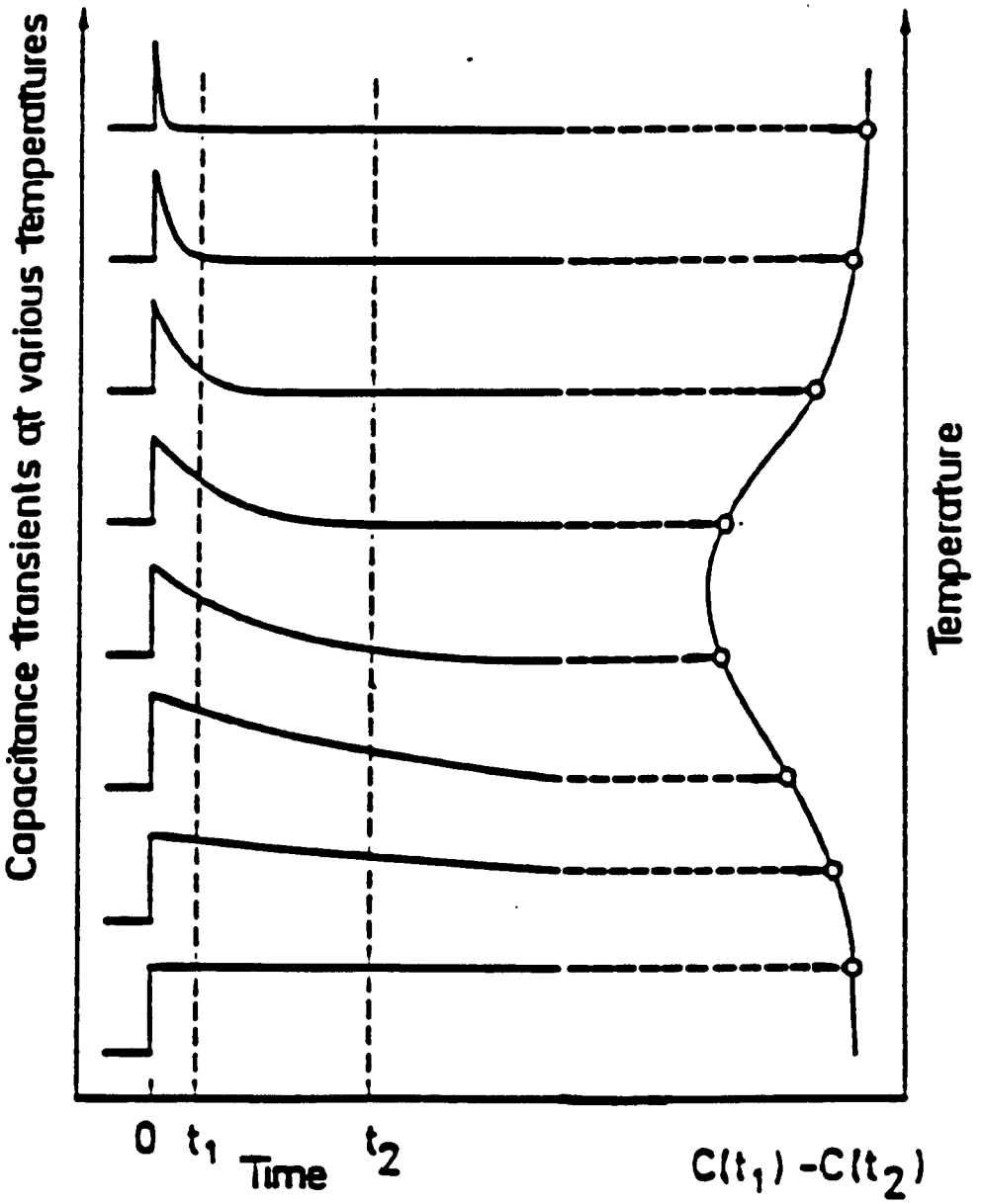

Figure 32. Illustration of the DLTS signal resulting from a changing capacitance transient with respect to temperature for a given rate window.

levels. Two of the diodes were found to have an abnormally large trap density. These large concentration of traps can be correlated to forward I-V-T results. The DLTS data from these 2 diodes will be presented, analyzed, and compared to the corresponding forward I-V-T plots.

The DLTS signals from these two diodes are shown in Figures 33(c) and 34(c). The DLTS signal has been defined as $[C(t_2) - C(t_1)]$, where the different t_1 and t_2 values are expressed in terms of the rate windows given by

$$RW = \frac{Ln\left(\frac{t_2}{t_1}\right)}{t_2 - t_1}. \qquad (4.12)$$

The two times, t_1 and t_2, have set ratios of 2, 5, and 10 with respect to each other. The times and corresponding rate windows used are listed in TABLE 2. The change in the capacitance is measured at the beginning, RW (1)-(3), and at the end, RW (4)-(6), of the transient. The rate windows that correspond to the largest time spacing, (3) and (6), give the best signal to noise ratio, but the worst resolution. Conversely, the small time spacing, RW (1) and (4), give poor signal to noise ratio and good resolution as seen in Figure 33(c) where (6) indicates two trap levels, but (4) gives better resolution of the two trap levels.

Table 2: Rate Windows and Times Used for Taking DLTS Data

	Rate Window (1/s)	t1 (ms)	t2 (ms)
1	693.1	1	2
2	402.4	1	5
3	255.8	1	10
4	28.6	48	24
5	41.6	48	9.6
6	52.9	48	4.8

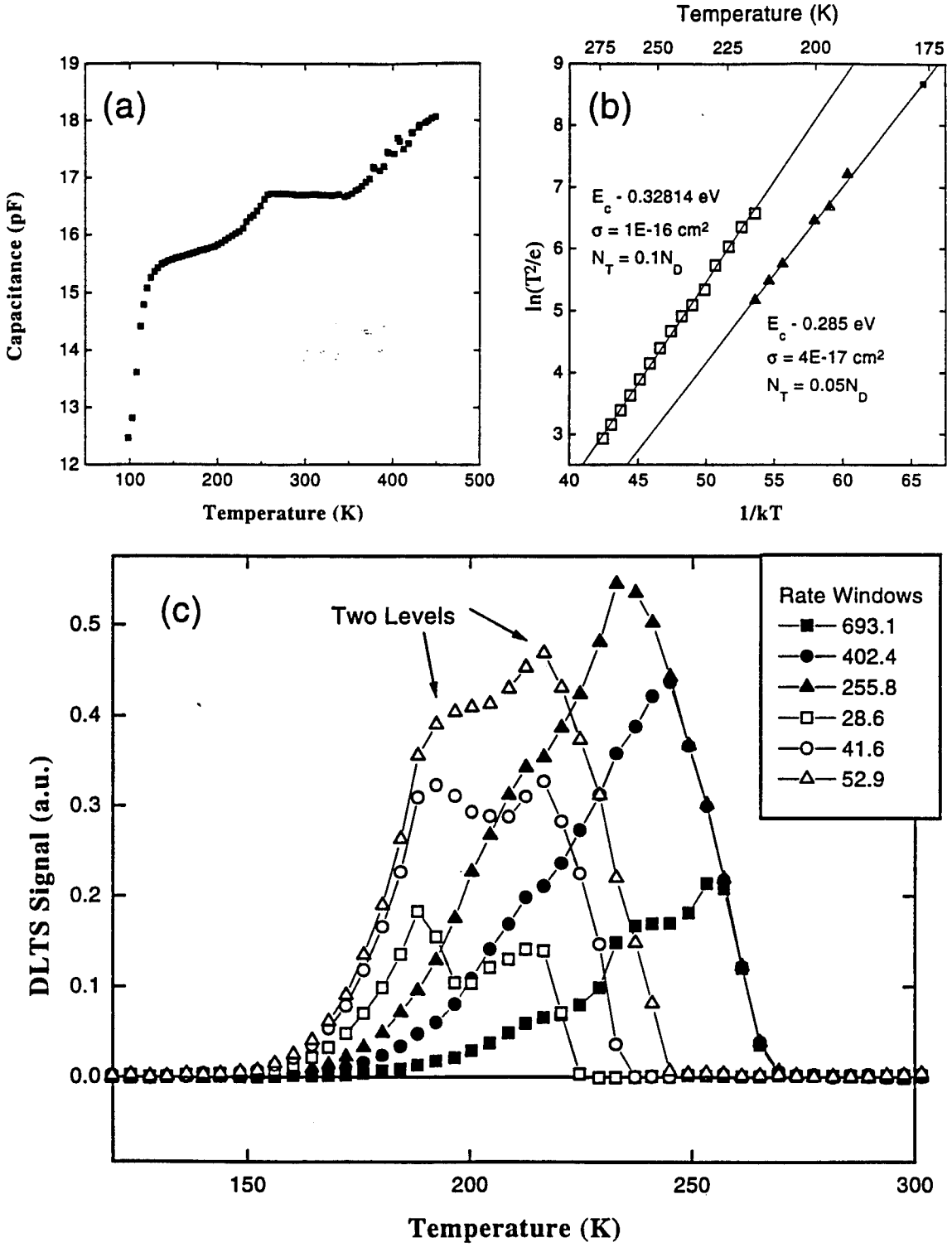

Figure 33. DLTS results for a p^+n diode, (a) C-T plot (b) Arrenhius plot used to determine the trap concentration, energy, and cross section (c) DLTS signal vs. temperature.

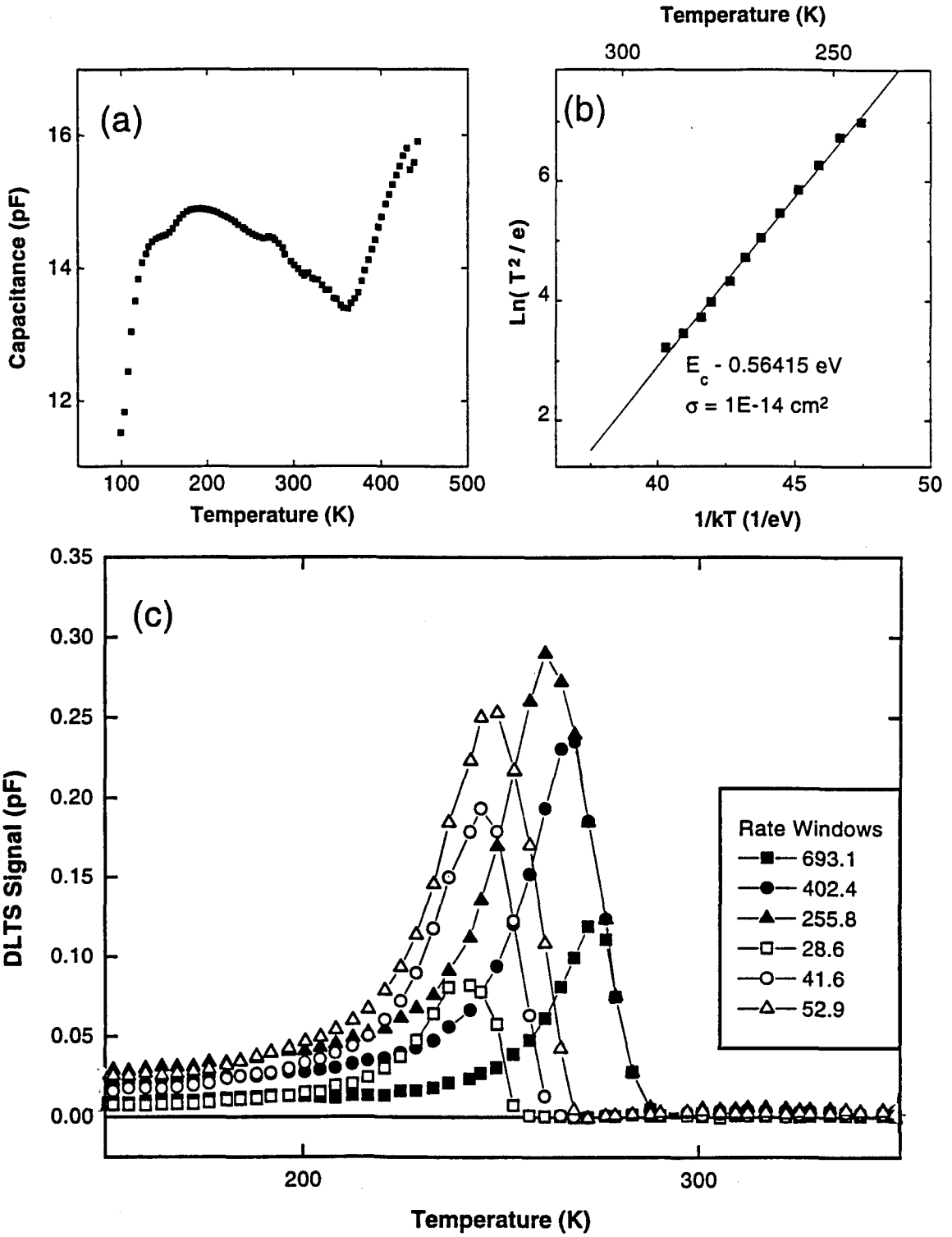

Figure 34. DLTS results for a p^+n diode (a) C-T plot (b) Arrenhius plot used to determine the trap concentration, energy, and cross section, and (c) DLTS signal vs. temperature.

One, two, or three emission rates are fit to each capacitance transient. With an Arrenhius plot of $Ln(T^2/e)$ vs. 1/kT, the results of this fit can be used to determine the activation energy and cross section as shown in Figures 33(b) and 34(b). The emission rate used in this calculation is given by

$$e = N_c \sigma \langle v \rangle \exp\left(\frac{-E_t}{kT}\right) \tag{4.13}$$

where E_t is measured from the conduction or valence band to the trap energy level for an n-side majority or minority trap, respectively. Figure 33(b) yielded two traps having activation energies of 328 and 285 meV, cross sections of $1x10^{-16}$ and $4x10^{-17}$ cm^{-2}, and concentrations of $0.1N_D$ and $0.05N_D$, respectively. The finding of two trap levels in Figure 33(b) and (c) is verified by the capacitance vs. temperature results shown in Figure 33(a), where the two steep increases in capacitance can be attributed to electron emission from majority carrier traps as explained previously in the C-V-T section. The second diode shown in Figure 34 was found to have a trap level at 564 meV with an abnormally large cross section of $1x10^{-14}$. However a capacitance vs. temperature plot shown in Figure 34(a) for this diode warrants further explanation.

As seen previously, the capacitance in Figure 34(a) increases rapidly around 100 K due to ionization freeze-out of donor levels. However, from 200-375 K the capacitance decreases. Although this phenomenon was not previously seen in the C-V-T results, it can be explained using the multi-phonon emission model, which expresses the capture cross section in Eq. (2.17) as

$$\sigma = \sigma_o \exp\left(\frac{-E_B}{kT}\right). \tag{4.14}$$

Here, E_B is a trap energy barrier height caused by electron coloumbic shielding of the trap nucleus. Calculations performed by Mr. Jim Scofield have found that the energy barrier for the diode depicted in Figure 34 is 220 ± 80 meV. At low temperatures the trap levels are empty due to the large barrier and the corresponding low capture rate. As higher temperature increases the capture cross section, electron capture occurs decreasing the capacitance. Up until 375 K electron capture dominates over electron emission. As the cross section continues to increase with increasing temperature the emission rate increases proportionally as does the number of filled trap. At ~375 K the capacitance reaches a minimum. At this point the defect levels are at a temperature where the maximum number of electrons are trapped, and qualitatively it can be stated that the emission and capture rates have an equal slope with respect to temperature. As temperature is increased past 375 K the thermal energy barrier becomes negligible and emission processes dominate causing the increase in capacitance with respect to temperature. The forward I-V-T curves of these two diodes are presented in Figure 35, where large tunneling and recombination currents reaffirm the correlation between poor diode performance and large trap concentrations.

Reverse Breakdown Measurements

The results of reverse breakdown measurements were found to be informative. A 100 MΩ resistor was put in series with the diode being tested in order to limit current once breakdown occurred. While this resistor did limit the current at device breakdown,

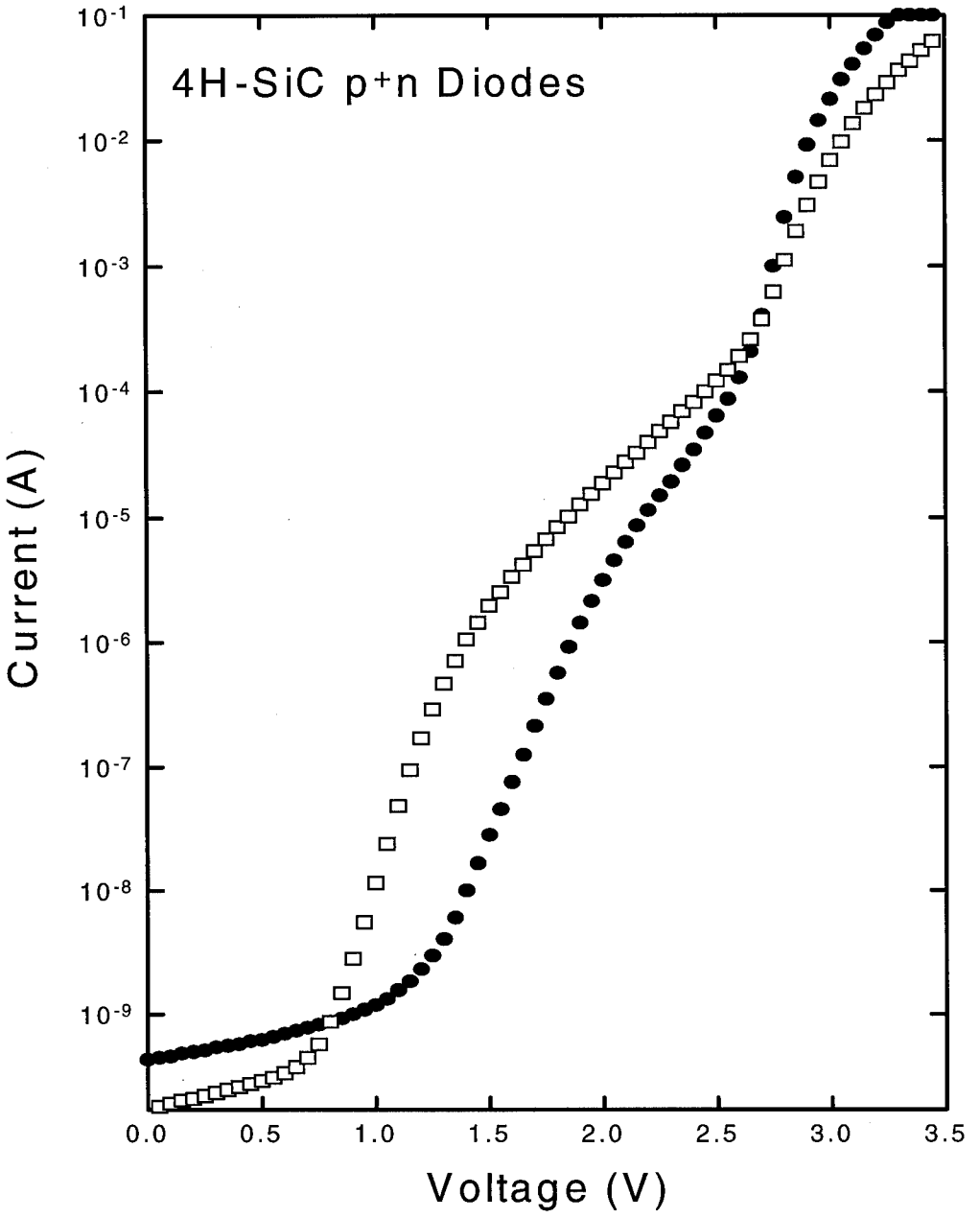

Figure 35. Forward I-V curves of two leaky diodes, where the high tunneling currents can be directly correlated to large trap concentrations.

it did not keep the diodes from being damaged. For a typical well-behaved diode the reverse current is ~1 μA at a reverse voltage of 300-350 V. Slowly increasing the reverse voltage resulted in a relatively constant reverse current slope up to 400-500 V, at this point the well-behaved diode would breakdown without warning. After breakdown, the 100 MΩ resistor succeeded in limiting current to ~ 4μA. Despite these low currents, a check of the forward I-V curve showed that the tested diodes had become leaky. Subsequent reverse breakdown tests on the same diode yielded lower and lower breakdown voltages with each trial. Mysteriously, during reverse I-V-T tests an average or leaky diode's characteristics would become suddenly worse and begin yielding inconsistent results. Later upon inspecting the reverse I-V-T data it was found that these diodes were beginning to breakdown. An example of this is shown below in Figure 36., where after taking the 350 K curve the diode ceased to give consistent results, and further data was not saved. Figure 37 shows a series of reverse I-V-T data where the diode did not begin to breakdown until 650 and 700 K. Recall from theory that a decreasing breakdown voltage with increasing temperature is caused only by breakdown due to tunneling. It is believed that the mysterious and sudden breakdown of the well-behaved diodes is due to so called micropipe or nanopipe bulk defects that are known to be present in this material. Therefore, the breakdown is not due to classical bulk avalanche breakdown, but due to a defect related mechanism.

The continual changing of a diode's characteristics with each reverse breakdown was not conducive to taking detailed breakdown data, or to doing many reverse

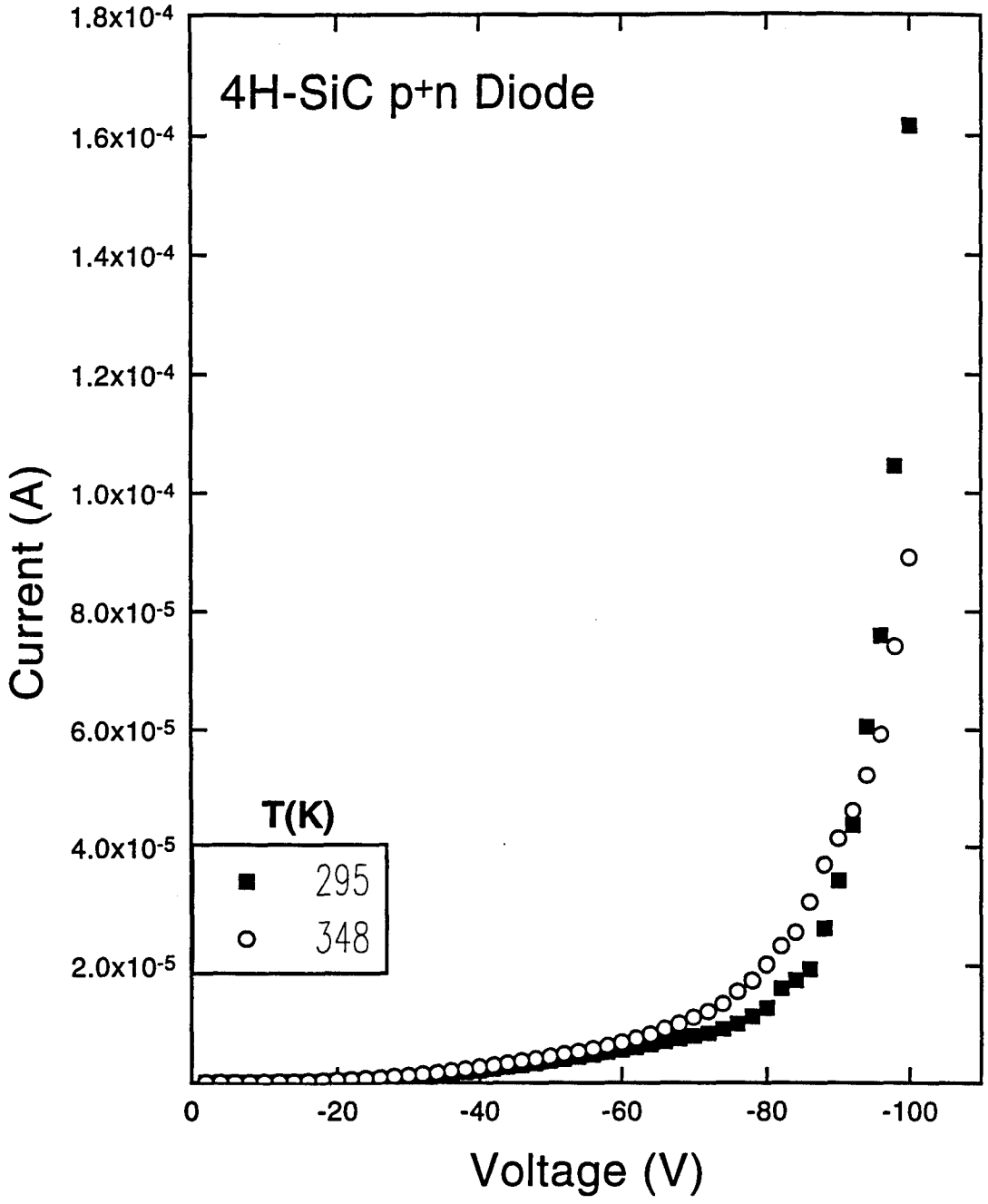

Figure 36. Reverse I-V-T data showing a leaky diode breaking down at ~ 95V.

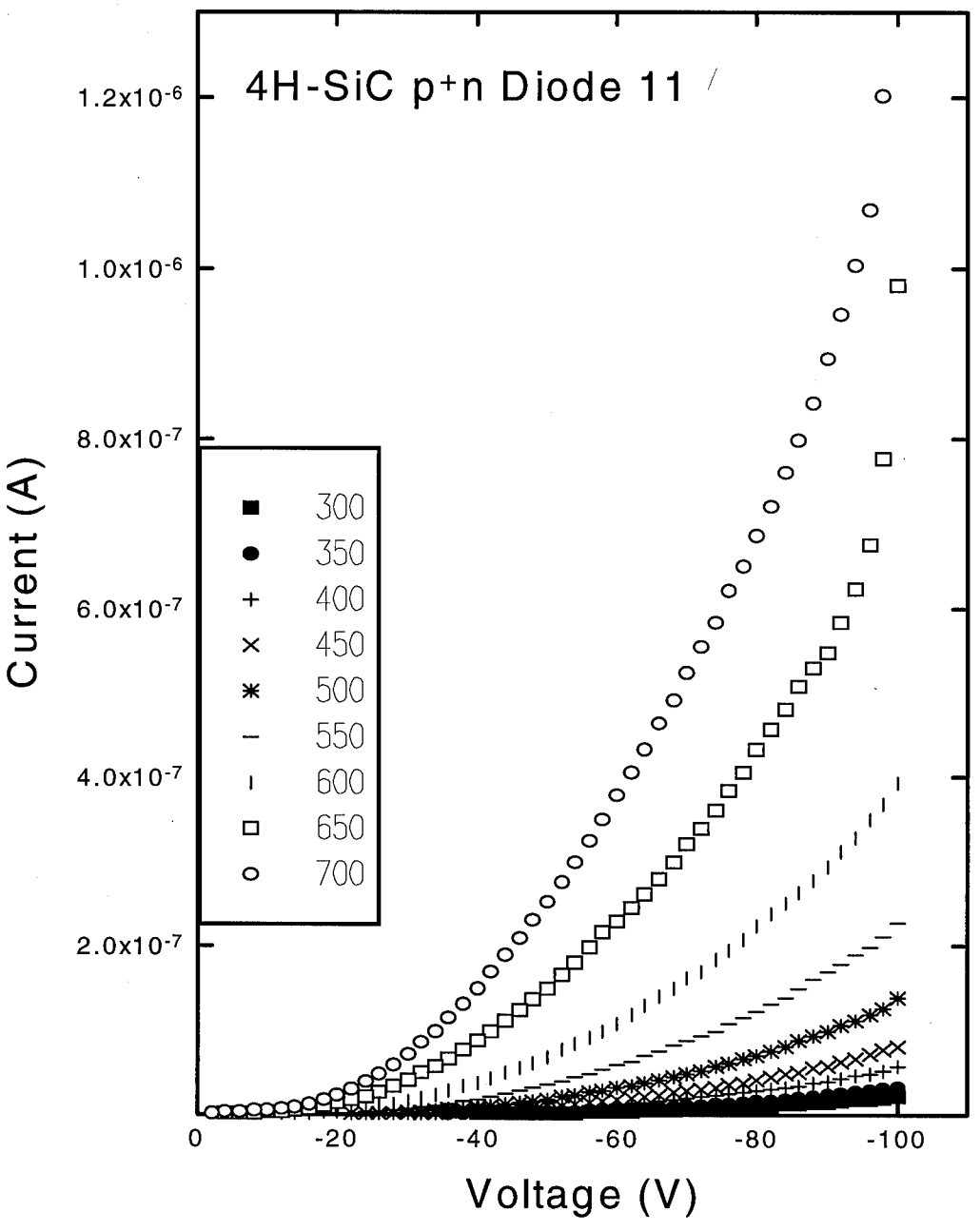

Figure 37. Reverse I-V-T data where junction breakdown begins to occur at higher temperatures, indicating tunneling breakdown.

breakdown tests, since the test effectively destroys the diode. Testing 7 well-behaved diodes yielded an average room temperature breakdown of 475 ± 47 volts, while reverse I-V-T data and reverse breakdown tests on leaky diodes yielded an average breakdown of ~95 volts.

Optical Observations

It was found that around 3 volts, blue light emitted via carrier recombination became intense enough to be viewed with the unaided eye. Qualitative observations found that well-behaved diodes emitted a uniform blue-violet ring of light from the junction, while the light emitted by a leaky diode had discrete sections where blue and/or green light was emitted. The emission of blue-green radiation from leaky diodes qualitatively indicate carrier recombination through defect levels within the bandgap.

V. Conclusions

The 4H-SiC p^+n diodes' characteristics were in general found to agree with established p-n junction I-V-T and C-V-T theory. Of the 28 diodes studied using I-V-T techniques, 12 were found to be well-behaved exhibiting a minimum amount of tunneling current and high reverse voltage breakdowns. Ten were classified as very poor, where recombination and tunneling were the dominant current processes at all voltages, and tunneling breakdown occurred at voltages as low as 100 V. The remaining 6 diodes were average. For well-behaved diodes, forward I-V-T data showed current conduction due to tunneling below 2 V, recombination between 2 and 2.5 V, and diffusion processes above 2.5 V. Series resistance was found to be a limiting factor around 2.75 V. Recombination currents yielded an activation energy of 1.56 eV and A_2 values of 1.85-2.1 compared to the ideal activation energy of 1.6 eV with A_2=2. The recombination-to-diffusion ratio for these diodes was also shown to agree well with theory. Reverse I-V-T data yielded a range of activation energies, but consistently indicated that reverse recombination currents are flowing through defect sites at ~70 meV, while low temperature C-V-T data yielded an activation energy level of 55 ± 11 meV. It is suspected that these are the same level, and this level can be attributed to the nitrogen donor levels.

By comparing C-V-T, I-V-T, and DLTS data for diodes 16, 17, and 18, an n-side majority carrier trap was positively identified. Reverse I-V-T data for the three diodes were used to calculate an activation energy of 173 ± 19 meV. C-V-T data for the three diodes showed a systematic arrangement of the diodes with respect to capacitance values, where diode 16 consistently had the largest capacitance of the three followed by diode 18

and finally diode 17 with the smallest capacitance. The larger capacitance of diode 18 was either attributable to a greater number of majority carrier traps or a smaller number of minority carrier traps. Examining forward I-V-T data for the diodes showed that diode 17 was the leakiest followed by diode 18 and diode 16, a well-behaved diode. The fact that the leakiest diode had the largest capacitance led to the conclusion that the energy trap at 173 ± 19 meV is a majority carrier trap. This conclusion was re-confirmed by DLTS and $1/C^2$ vs. V results. $1/C^2$ vs. V plots gave experimentally determined doping density profiles which agreed with the manufacturer's specification. Of 10 diodes tested using the DLTS technique, 5 yielded a majority trap level at 150 ± 34 meV with concentrations on the order of $1x10^{13}$ cm^{-3}. It is believed that this is the same level seen with reverse I-V-T techniques.

Reverse breakdown measurements on leaky and well-behaved diodes found typical reverse bias breakdown voltages of ~95 and ~475 Volts, respectively. The decrease of the breakdown voltage with increasing temperature leads to the conclusion that tunneling breakdown, as opposed to avalanche breakdown, is occurring. Some well-behaved diodes exhibited breakdown at unexpectedly low reverse voltages. This unexpected breakdown can be attributed to nanopipe defects which allow large tunneling currents to flow. Until the nanopipe problem is completely solved silicon-carbide devices will be limited in size and quality.

Future research with 4H-SiC should entail looking at the diode spectrum with a spectrometer. The qualitative observations of the radiation emitted from the diodes indicated an avenue for future work, where spectroscopy measurements could be used in conjunction with other methods to gain more knowledge about the recombination centers

in 4H-SiC. A second avenue for future research is the study of reverse recombination currents at different test chamber pressures. It is suspected that reverse surface recombination currents will change with atmospheric pressure. Finding the pressure at which these currents are minimized could lead to devices that are hermetically packaged at a pressure to yielding optimum performance.

Scofield, James D. "Electrical Characterization of Acceptor-Impurity Induced Bulk and Interface States in Hexagonal SiC." Unpublished Doctoral Prospectus. The Air Force Institute of Technology, Graduate School of Engineering, Wright-Patterson AFB OH. December, 1993.

Scofield, James D. Private Communications, The Air Force Institute of Technology, Graduate School of Engineering, Wright-Patterson AFB OH. 15-30 September, 1995.

Shah, N.M., "More Electric F-18 Cost Benefits Study, WL-TR-91-2093, 1992, Northrop Corporation, Aircraft Division.

Shockley, W. "The Theory of p-n Junctions in Semiconductors and p-n Junction Transistors," Bell Syst. Tech. J. **28,** 435 (1949); Compilation by S.M. Sze. Semiconductor Devices: Pioneering Papers. New Jersey: World Scientific, 1991.

Shockley, W., and Read, W.T. Jr., "Statistics of the Recombination of Holes and Electrons," Phys. Rev. **87,** 835 (1949); Compilation by S.M. Sze. Semiconductor Devices: Pioneering Papers. New Jersey: World Scientific, 1991.

Sze, S.M. Physics of Semiconductor Devices, (Second Edition). New Jersey: John Wiley & Sons, 1981.

Sze, S.M. Semiconductor Devices Physics and Technology. New Jersey: John Wiley & Sons, 1985.

Tan, C., and Xu, M., Solid St. Electron. **32**, 25 (1989).

Wang, S., Dudley, M., Carter C., Ashbury, D., and Fazi, C., "Characterization of Defect Structures in SiC Single Crystals Using Synchrotron X-ray Topography," Materials Res. Soc. Symposia Proc., **307**, Applicat. of Synchrotron Radiation Techniques to Materials Sci., D. L. Perry, N.D. Shinn and others, Eds. Pittsburgh: Materials Research Society, 1993.

Wolf, G., Noel, G.T., and Stirn, R.J., IEEE Trans. on Electron. Dev. **24,** 419 (1977).

Vita

Michael E. Dunn [redacted] His family moved to Hayden Lake, Idaho in 1975 where he resided until graduating from Coeur d' Alene High School in May 1990. He accepted an appointment and entered the US Air Force Academy in June 1990. In Colorado he gained a love for rock climbing and backpacking in the Rocky Mountains. He graduated in 1994 with a Bachelor of Science in Physics and after receiving a regular commission in the USAF was assigned to the Air Force Institute of Technology Graduate School of Engineering to work towards a Master of Science in Engineering Physics. As of writing this he does not have a follow-on assignment, but he is dreaming of going to a place where the research is interesting and the mountains are big.

REPORT DOCUMENTATION PAGE

Form Approved
OMB No. 0704-0188

1. AGENCY USE ONLY *(Leave blank)*	2. REPORT DATE	3. REPORT TYPE AND DATES COVERED
	December 1995	Master's Thesis

4. TITLE AND SUBTITLE
Electrical Characterization of 4H-Silicon Carbide P-N Junction Diodes

5. FUNDING NUMBERS

6. AUTHOR(S)
Michael E. Dunn
2nd Lt, USAF

7. PERFORMING ORGANIZATION NAME(S) AND ADDRESS(ES)
Air Force Institute of Technology, WPAFB OH 45433-6568

8. PERFORMING ORGANIZATION REPORT NUMBER
AFIT/GAP/ENP/95D-04

9. SPONSORING / MONITORING AGENCY NAME(S) AND ADDRESS(ES)
Dr. Kitt C. Reinhardt
WL/POOC
Wright-Patterson AFB, OH. 45433-6543

10. SPONSORING / MONITORING AGENCY REPORT NUMBER

11. SUPPLEMENTARY NOTES

12a. DISTRIBUTION / AVAILABILITY STATEMENT
Approved for public release; Distribution Unlimited

12b. DISTRIBUTION CODE
A

13. ABSTRACT *(Maximum 200 words)*

The current conduction mechanisms of 4H-SiC p^+n mesa diodes were studied using current-voltage-temperature (I-V-T), capacitance-voltage-temperature (C-V-T), deep level transient spectroscopy (DLTS), optical observations, and reverse breakdown measurements. Temperature and voltage dependencies of diffusion, recombination, and tunneling current processes are shown to be consistent with Sah-Noyce-Shockley theory. Recombination currents having an ideality factor of A=1.85-2.1 yielded an activation energy of E_A=1.56 eV, whereas for ideal recombination, A=2 and E_A=1.6 eV. Forward I-V curves of poor diodes dominated by tunneling and recombination processes, showing low reverse breakdown voltages of ~100 V, can be correlated to DLTS results which show large defect concentration. On the other hand, well-behaved diodes exhibited a breakdown voltage at ~450 V, and recombination-to-diffusion current ratios of 10^{12}-10^{29} that agree with theory. C-V-T, DLTS, and reverse I-V-T data revealed several defect centers. C-V-T and reverse I-V-T measurements yielded an energy level at ~70 and ~62 meV, respectively, which is possibly attributable to nitrogen donor levels. Reverse I-V-T and DLTS results, in approximately half of the diodes tested, yielded a seconded trap level at 173 ± 19 and 150 ± 34 meV, respectively.

14. SUBJECT TERMS
Diodes, Silicon-Carbide, 4H, Electrical Characterization, p-n Junction, Current Conduction

15. NUMBER OF PAGES
98

16. PRICE CODE

17. SECURITY CLASSIFICATION OF REPORT	18. SECURITY CLASSIFICATION OF THIS PAGE	19. SECURITY CLASSIFICATION OF ABSTRACT	20. LIMITATION OF ABSTRACT
UNCLASSIFIED	UNCLASSIFIED	UNCLASSIFIED	UL

GENERAL INSTRUCTIONS FOR COMPLETING SF 298

The Report Documentation Page (RDP) is used in announcing and cataloging reports. It is important that this information be consistent with the rest of the report, particularly the cover and title page. Instructions for filling in each block of the form follow. It is important to ***stay within the lines*** to meet ***optical scanning requirements***.

Block 1. Agency Use Only *(Leave blank)*.

Block 2. Report Date. Full publication date including day, month, and year, if available (e.g. 1 Jan 88). Must cite at least the year.

Block 3. Type of Report and Dates Covered. State whether report is interim, final, etc. If applicable, enter inclusive report dates (e.g. 10 Jun 87 - 30 Jun 88).

Block 4. Title and Subtitle. A title is taken from the part of the report that provides the most meaningful and complete information. When a report is prepared in more than one volume, repeat the primary title, add volume number, and include subtitle for the specific volume. On classified documents enter the title classification in parentheses.

Block 5. Funding Numbers. To include contract and grant numbers; may include program element number(s), project number(s), task number(s), and work unit number(s). Use the following labels:

C	- Contract	**PR**	- Project
G	- Grant	**TA**	- Task
PE	- Program Element	**WU**	- Work Unit Accession No.

Block 6. Author(s). Name(s) of person(s) responsible for writing the report, performing the research, or credited with the content of the report. If editor or compiler, this should follow the name(s).

Block 7. Performing Organization Name(s) and Address(es). Self-explanatory.

Block 8. Performing Organization Report Number. Enter the unique alphanumeric report number(s) assigned by the organization performing the report.

Block 9. Sponsoring/Monitoring Agency Name(s) and Address(es). Self-explanatory.

Block 10. Sponsoring/Monitoring Agency Report Number. *(If known)*

Block 11. Supplementary Notes. Enter information not included elsewhere such as: Prepared in cooperation with...; Trans. of...; To be published in.... When a report is revised, include a statement whether the new report supersedes or supplements the older report.

Block 12a. Distribution/Availability Statement. Denotes public availability or limitations. Cite any availability to the public. Enter additional limitations or special markings in all capitals (e.g. NOFORN, REL, ITAR).

- **DOD** - See DoDD 5230.24, "Distribution Statements on Technical Documents."
- **DOE** - See authorities.
- **NASA** - See Handbook NHB 2200.2.
- **NTIS** - Leave blank.

Block 12b. Distribution Code.

- **DOD** - Leave blank.
- **DOE** - Enter DOE distribution categories from the Standard Distribution for Unclassified Scientific and Technical Reports.
- **NASA** - Leave blank.
- **NTIS** - Leave blank.

Block 13. Abstract. Include a brief *(Maximum 200 words)* factual summary of the most significant information contained in the report.

Block 14. Subject Terms. Keywords or phrases identifying major subjects in the report.

Block 15. Number of Pages. Enter the total number of pages.

Block 16. Price Code. Enter appropriate price code *(NTIS only)*.

Blocks 17. - 19. Security Classifications. Self-explanatory. Enter U.S. Security Classification in accordance with U.S. Security Regulations (i.e., UNCLASSIFIED). If form contains classified information, stamp classification on the top and bottom of the page.

Block 20. Limitation of Abstract. This block must be completed to assign a limitation to the abstract. Enter either UL (unlimited) or SAR (same as report). An entry in this block is necessary if the abstract is to be limited. If blank, the abstract is assumed to be unlimited.